Geomorphology xxx (2013) xxx–xxx

Contents lists available at SciVerse ScienceDirect

Geomorphology

journal homepage: www.elsevier.com/locate/geomorph

Co-seismic, geomorphic, and geologic fold growth associated with the 1978 Tabas-e-Golshan earthquake fault in eastern Iran

R.T. Walker [a,*], M.M. Khatib [b], A. Bahroudi [c,d], A. Rodés [e], C. Schnabel [e], M. Fattahi [f,g], M. Talebian [c], E. Bergman [h]

[a] Department of Earth Sciences, University of Oxford, Parks Road, Oxford OX1 3PR, UK
[b] Department of Geology, Birjand University, Birjand, Iran
[c] Geological Survey of Iran, Azadi Square, Meraj Avenue, P.O. Box 11365-4563, Iran
[d] Mining Engineering Faculty of the Engineering University College, University of Tehran, Kargar Shomali, Tehran, Iran
[e] NERC Cosmogenic Isotope Analysis Facility, East Kilbride G75 0QF, UK
[f] Institute of Geophysics, University of Tehran, Kargar Shomali, Tehran, Iran
[g] School of Geography, University of Oxford, South Parks Road, Oxford OX1 3QY, UK
[h] Center for Imaging the Earth's Interior, Department of Physics, University of Colorado at Boulder, 390 UCB, CO 80309, USA

ARTICLE INFO

Article history:
Received 30 March 2012
Received in revised form 19 February 2013
Accepted 22 February 2013
Available online xxxx

Keywords:
Folding
Thrust faulting
Iran
Alluvial fans
Holocene
Earthquake

ABSTRACT

We describe the seismicity and late Cenozoic deformation associated with a blind thrust fault at Tabas-e-Golshan (hereafter referred to as Tabas), eastern Iran, which generated a devastating M_w 7.3 earthquake on the 16th September 1978. Measurements from a structural transect through the Sardar anticline segment indicate fault-propagation folding above a gently ~20° eastward-dipping blind thrust fault. The thrust flattens into a horizontal detachment at a depth of only ~2 km. Tightening of the fold forelimb is accommodated by flexural slip along numerous bedding planes, with many of the slip surfaces showing fresh striations with a large component of right-lateral strike–slip. A steeply dipping fault zone showing almost pure strike–slip is also developed within the forelimb of the fold. Our field observations are consistent with the source parameters of the 1978 Tabas earthquake, and additional events in 1979 and 1980, which all involved slip on a shallowly-dipping thrust with a significant component of right-lateral slip. The surface of an alluvial fan, which is likely to have been abandoned at 8–10 ka, has been folded as it crosses the Sardar anticline. The age constraints, combined with topographic profiles along the deformed fan surface and constraints on the dip of the fault at depth, provide an approximate rate of horizontal shortening of ~1.5 mm/yr. Shortening at Tabas appears to result from transpressional bending at the north end of the Nayband strike–slip fault. A northward continuation of the Nayband Fault, which may be slipping at rates of >2 mm/yr, is identified along the base of the Shotori Mountains ~10–20 km east of the Tabas thrust. The range-front fault did not move in 1978 and constitutes an additional threat to local populations.

1. Introduction

On September 16, 1978, the oasis town of Tabas in eastern Iran was destroyed, and ~20,000 people were killed, by an earthquake of M_w 7.3 (Berberian, 1979; Fig. 1). This earthquake, which occurred on a series of previously unrecognised blind thrust faults, was one of the largest and most destructive to have occurred in Iran in recent decades. Despite having a long history of occupation, there are no records of destructive earthquakes in the area prior to 1978 (e.g. Berberian, 1979; Ambraseys and Melville, 1982). Evidence of long-term active faulting is, however, preserved in the landscape in the form of anticlinal folding in Neogene basin deposits, deformation of late Quaternary alluvial fan deposits, and widespread river incision (Walker et al., 2003). No estimates exist of the rate of slip, and hence the average interval between large earthquakes, on the Tabas Fault system.

The Tabas folds, and presumably the thrust faults that underlie them, are segmented (Fig. 2). For the purposes of this study we focus primarily on the segment located close to the Sardar River in the northern part of the system (Fig. 3). We choose this segment for three reasons. (1) The Sardar fold is the only visible fold segment present at this latitude; farther south, several parallel folds appear to be active simultaneously, thus making shortening estimates much more difficult to determine. (2) Uninterrupted exposures of folded and faulted strata outcrop along the walls of the deeply incised Sardar River allowing a detailed structural cross-section to be produced. (3) The Sardar River is incised into the surface of a large alluvial fan, which is continuous across the fold, and, when combined with estimates of its age, can be used to determine a rate of shortening across the fold.

* Corresponding author.
E-mail address: richard.walker@earth.ox.ac.uk (R.T. Walker).

0169-555X/$ – see front matter © 2013 Published by Elsevier B.V.
http://dx.doi.org/10.1016/j.geomorph.2013.02.016

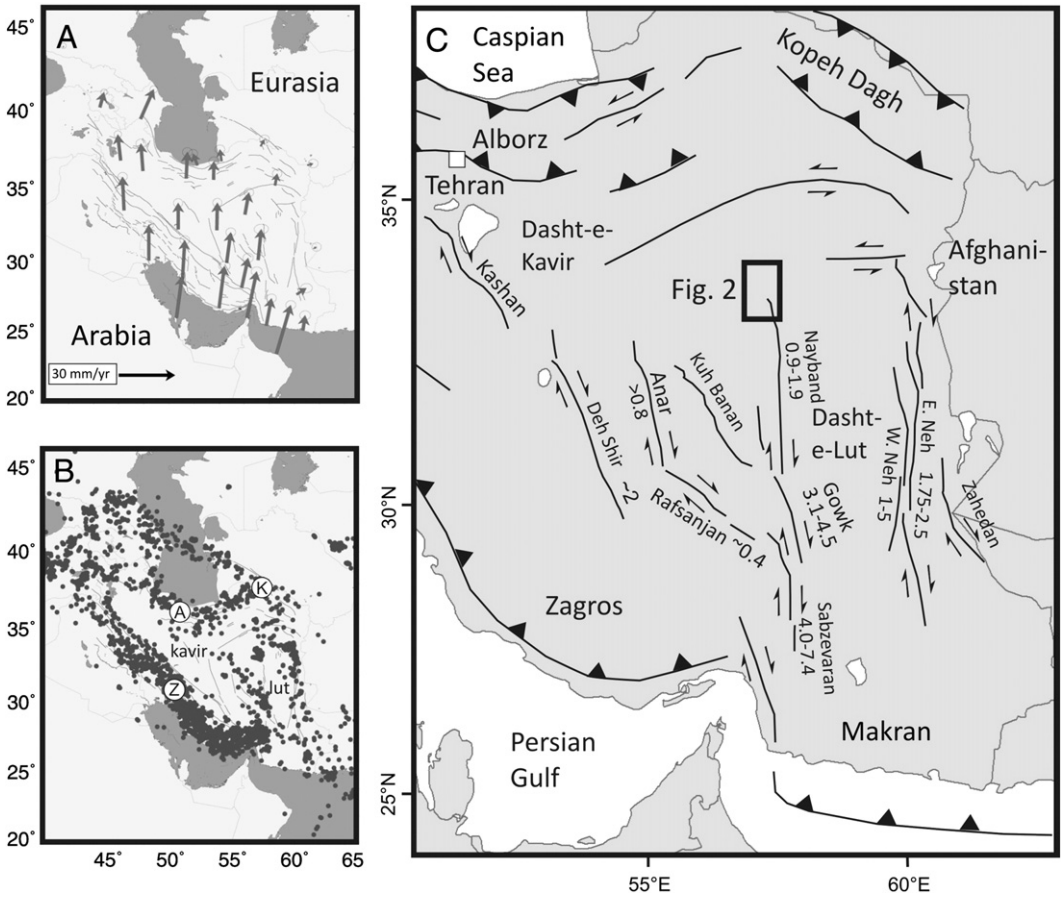

Fig. 1. (A) GPS velocities of points within Iran relative to Eurasia (Vernant et al., 2004). (B) Epicentres of earthquakes (Mw > 5.3) in Iran from the catalogue of Engdahl et al. (1998). Much of the seismicity is located within the Zagros Mountains (Z) in the south, and the Alborz (A) and Kopeh Dagh (K) ranges in the north. The Kavir and Lut deserts have fewer earthquakes within them. (C) Map of Iran showing the locations and estimated slip-rates (in mm/yr) of the major strike–slip faults in eastern Iran (from Regard et al., 2005; Meyer et al., 2006; Meyer and LeDortz, 2007; Le Dortz et al., 2009; Walker et al., 2009, 2010; Le Dortz et al., 2011; Fattahi et al., 2011). The Tabas reverse faults are situated at the northern end of the Nayband Fault (the boxed region is shown in more detail in Fig. 2).

In the following sections, we first describe the tectonic setting of the Tabas earthquake. To aid our description of the earthquake we present improved epicentres of seismicity in the Tabas region obtained from a multiple-event relocation technique. We then use the deformation of an alluvial fan crossing the Sardar fold segment, combined with age constraints from luminescence and cosmogenic ^{36}Cl exposure dating on the abandonment of the fan surface, to estimate a rate of uplift across the underlying fault. With constraints on the dip of the Tabas Fault at depth (obtained from seismology and a structural cross-section) we convert this rate of uplift into rates of horizontal shortening (important for regional tectonic studies) and a rate of slip along the fault (useful for estimating the average interval between earthquakes). Finally, we assess the implications of our study for the source processes of the 1978 earthquake, the tectonics of eastern Iran, and for the evolution of the landscape observed at the present-day near Tabas.

2. Tectonic setting

The active tectonics of Iran are controlled by the northward motion of Arabia, at a velocity of ~25 mm/yr at longitude 60°E, with respect to the interior of Eurasia (Fig. 1A; Vernant et al., 2004). Deformation resulting from this northward motion is broadly confined to within the political borders of Iran, and surrounding parts of Pakistan, Afghanistan and Turkmenistan appear to behave as non-deforming parts of stable Eurasia. Northward motion of central and northern Iran with respect to Afghanistan introduces a north–south right-lateral shear of ~15 mm/yr along the eastern border of Iran (Jackson and McKenzie, 1984; Vernant et al., 2004).

The north–south shear between Iran and Afghanistan is accommodated by several right-lateral strike–slip fault systems bordering the Dasht-e-Lut Desert (Fig. 1; Walker and Jackson, 2004; Meyer and LeDortz, 2007). The East Neh, West Neh and Zahedan faults follow the eastern margin of the Dasht-e-Lut. In the west, right-lateral shear is accommodated on the Sabzevaran–Gowk–Nayband Fault system (Walker and Jackson, 2002; Walker et al., 2010). Regard et al. (2005) estimate, from the ^{10}Be exposure dating of displaced alluvial fans, that the Jiroft–Sabzevaran Fault system in the southwest of the Dasht-e-Lut accommodates ~6 mm/yr of the 15 mm/yr of regional right-lateral shear. However, the slip-rate of faults bordering the western margin of the Dasht-e-Lut desert decreases northwards, with the Holocene slip-rate on the Gowk Fault estimated at 3.8 ± 0.7 mm/yr (Walker et al., 2010), and a slip-rate of 1.4 ± 0.5 mm/yr estimated on the Nayband Fault from ~2 Ma basalts displaced across it (Camp and Griffis, 1982; Walker et al., 2009). The epicentral zone of the 1978 Tabas earthquake is situated at the northern end of the Nayband Fault (Fig. 2).

3. Geology and geomorphology of the Tabas thrust fault system

The Tabas folds are situated between the Tabas playa depression (~600 m above sea level) and the Shotori Mountains, with peak elevations of ~2900 m (Fig. 2). The folds are expressed in the topography as a series of low rounded hills with no more than ~100 m of relief above

Please cite this article as: Walker, R.T., et al., Co-seismic, geomorphic, and geologic fold growth associated with the 1978 Tabas-e-Golshan earthquake fault in eastern Iran, Geomorphology (2013), http://dx.doi.org/10.1016/j.geomorph.2013.02.016

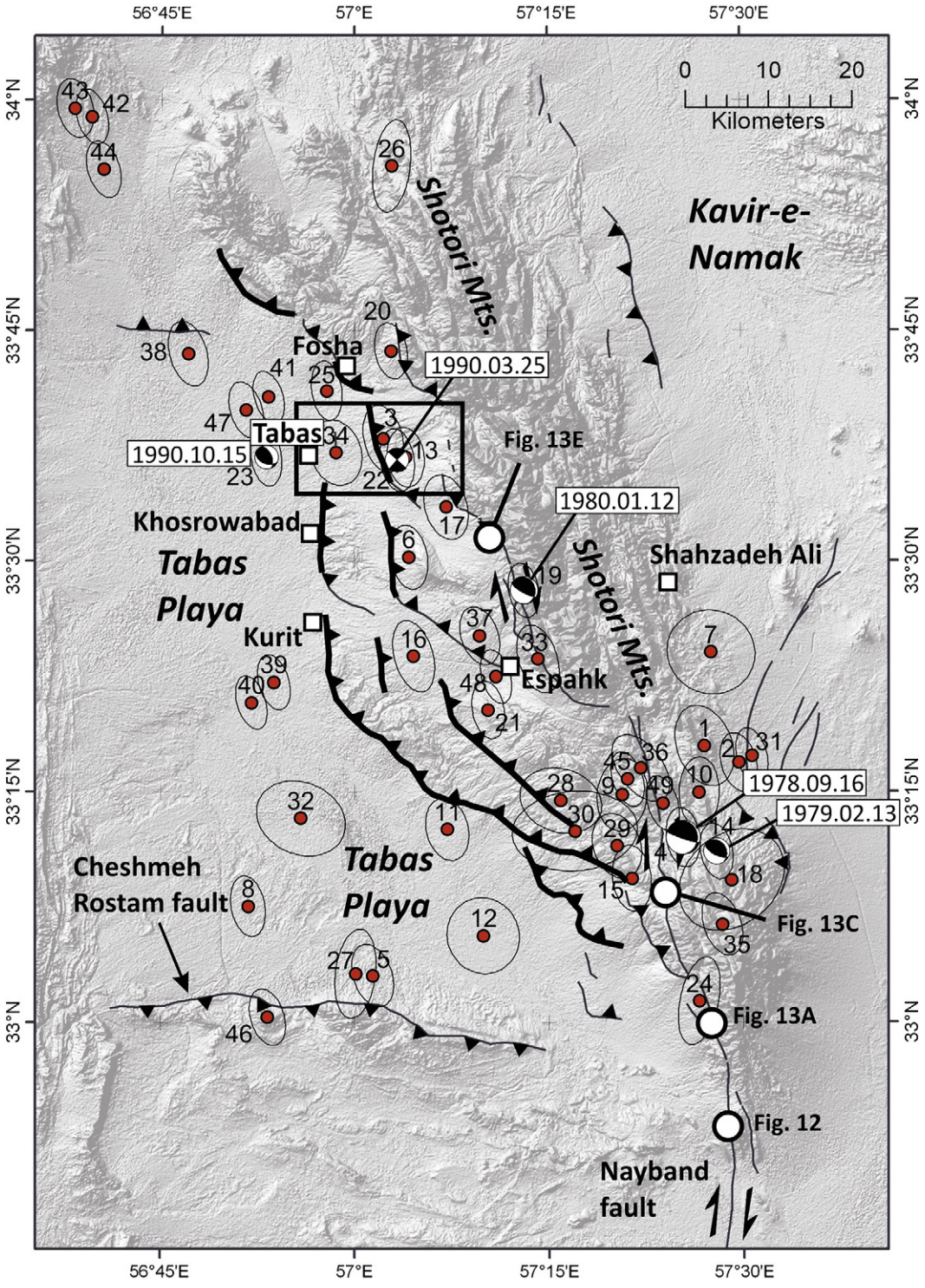

Fig. 2. ASTER GDEM digital topographic map of the Tabas region. Fault segments on which co-seismic surface ruptures were observed following the 1978 earthquake (Berberian, 1979) are represented by thickened fault lines; but note that much of the rupturing took the form of distributed faulting – caused by fold growth – within the hanging-walls of the underlying east-dipping reverse faults. It is possible that slip at depth occurred on additional segments within the Tabas system. Earthquake epicentres are relocated following the method described in Section 4.1 and are shown with their 90% confidence ellipses for absolute location. All earthquakes are numbered chronologically as in Table 1. Focal mechanisms for the 1978.09.16 Tabas earthquake (event no. 4), and events in 1979 and 1980 (events 14 and 19) are from body-waveform modelling (Walker et al., 2003). The two mechanisms from 1990 (events 22 and 23) are from the global CMT catalogue (http://www.globalcmt.org). Dots represent epicentres of smaller earthquakes. White circles represent sites shown in Figs. 12 and 13. The boxed area near Tabas town covers the Sardar fold segment and is shown in greater detail in Fig. 3.

the surrounding gravel apron. The Shotori Mountains are composed of heavily deformed Palaeozoic and Mesozoic rocks (Stöcklin and Nabavi, 1969). Changes in sediment thickness from the Shotori Mountains towards Tabas indicate several periods of fault reactivation since the late Pre-Cambrian, with a final, ongoing, phase of shortening initiating in the Late Tertiary (Stöcklin et al., 1965; Berberian, 1979). The present-day activity involves slip on eastward-dipping thrust faults that underlie the Tabas folds (Fig. 2; Berberian, 1979; Walker et al., 2003).

West of the Shotori Mountains, the late Cenozoic deposition is typified by a sequence of lakebed and fluvial marls grading upwards

Please cite this article as: Walker, R.T., et al., Co-seismic, geomorphic, and geologic fold growth associated with the 1978 Tabas-e-Golshan earthquake fault in eastern Iran, Geomorphology (2013), http://dx.doi.org/10.1016/j.geomorph.2013.02.016

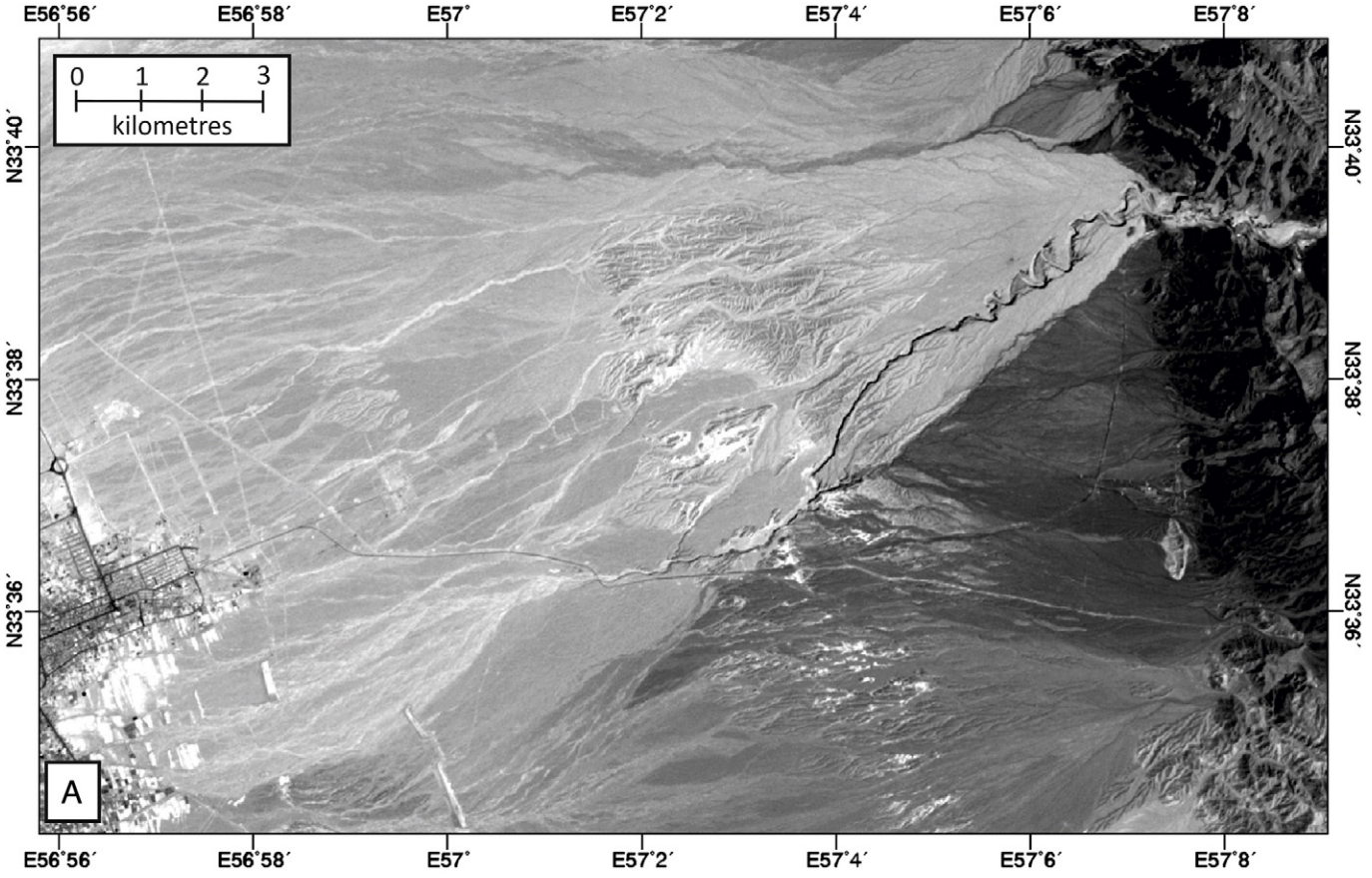

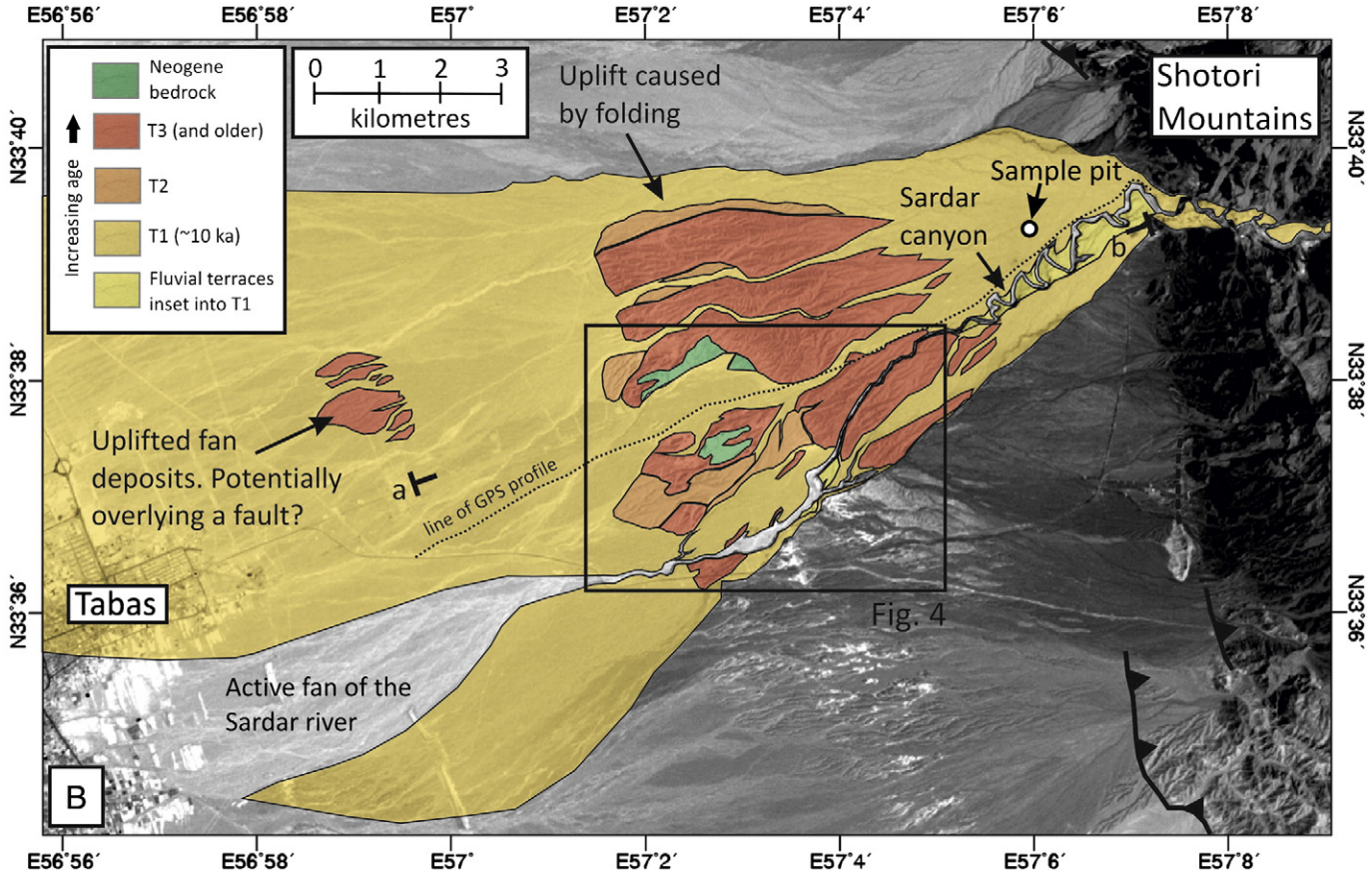

Please cite this article as: Walker, R.T., et al., Co-seismic, geomorphic, and geologic fold growth associated with the 1978 Tabas-e-Golshan earthquake fault in eastern Iran, Geomorphology (2013), http://dx.doi.org/10.1016/j.geomorph.2013.02.016

into conglomerate. The marls are exposed in the cores of the Tabas anticlines and produce light shades in LANDSAT imagery (Fig. 3). River terraces and laterally equivalent gravel fans are widespread both within both the Shotori Mountains and along the margins of the mountains. Large alluvial fans originating at the range-front have been deposited across the Tabas folds. The surfaces of these fans, which are probably late Quaternary in age, are often deeply incised by river canyons.

4. Seismicity of the Tabas region

The 16 September 1978 (Mw 7.3) Tabas earthquake is the largest instrumentally recorded earthquake in Iran. It devastated the entire region, killing 85% of the population of Tabas (e.g. Berberian, 1979). The earthquake occurred prior to the development of geodetic techniques for imaging earthquake ground deformation; though seismological, remote-sensing, and field investigations have all helped to develop a broad understanding of the Tabas earthquake as the result of slip on a series of eastward-dipping blind thrust faults (Berberian, 1979; Berberian et al., 1979; Niazi and Kanamori, 1981; Berberian, 1982; Silver and Jordan, 1983; Shoja-Taheri and Anderson, 1988; Walker et al., 2003; Sarkar et al., 2004). The rather complex, and apparently contradictory, surface faulting observed immediately after the earthquake (e.g. Berberian, 1979) is now recognised to result from fold growth above the blind faults (Walker et al., 2003). There are, however, still many features of the Tabas earthquake, and of its causative faults, that are unresolved.

One of the main aims of our paper is to help resolve some of these features by drawing observations together from geology, geomorphology and seismology. Below, we briefly review the available information on the Tabas earthquake. We also present improved epicentral locations of seismicity in the Tabas region that help to show the distribution of deformation within the region.

4.1. Epicentral locations

The epicentres of the Tabas main-shock and other regional seismicity shown in Fig. 2 have been relocated with the hypocentroidal decomposition (HDC) method for multiple event relocation (Jordan and Sverdrup, 1981), using a methodology that has been extensively developed and tested to determine earthquake locations for which scatter and bias have both been minimised. The HDC method separates the relocation procedure into two steps, solving for the relative location of each event in the cluster with respect to the 'hypocentroid' or geometrical centre of the cluster, and then solving for the absolute location of the hypocentroid, which establishes the locations of all cluster events in geographic coordinates and universal time. The key to obtaining locations with minimal bias ("calibrated" locations) is the careful selection of arrival time data (i.e., from short epicentral distances) to minimise the biasing effect of inadequately known velocity structure. An analysis of the scatter of repeated observations of the same phase at the same station allows us to apply empirical uncertainties to all readings and to identify (and remove) outlier readings, both of which are essential for obtaining reliable estimates of location uncertainty. The method has been applied in a number of studies, including several in Iran (e.g., Walker et al., 2005; Parsons et al., 2006; Tatar et al., 2007; Walker et al., 2011; Ghods et al., 2012).

For the Tabas study we formed a cluster of 49 instrumentally-recorded earthquakes from 1973 through 2010. Most events have magnitudes between 3.5 and 5.5 (usually m_b or M_L). The 1978 Tabas mainshock and its immediate aftershocks (~3 months) comprise about 1/3 of the cluster (16 events). Many of the events in the cluster were extracted from a database of earthquake locations in the Iran region, located with the EHB single-event location algorithm of Engdahl et al. (1998). The HDC method is not well suited to resolving event depths directly. For relocation, focal depths were held fixed at depths consistent with teleseismic depth phase arrivals (8–20 km) when they are available, and fixed at a depth of 12 km when there is no such constraint. The calibrated locations of all 49 events are presented in Table 1 and shown in Fig. 2. Calibration of the cluster was made using seismological constraints from stations at epicentral distances less than 2.6°. This is somewhat further than desirable but was necessary in this case to obtain adequate azimuthal coverage. Calibration of the hypocentroid was greatly aided by observations of the three events in 2010 by the recently installed TABS seismic station, which is very close (25–45 km) and which also provides critical azimuthal coverage for Pg. The 90% confidence ellipses shown in Fig. 2 are formed by adding the covariance matrix for the uncertainty of relative location for each event to that of the hypocentroid location (an ellipse with semi-axis lengths of 1.4 and 3.0 km), with scaling based on the empirical estimates of the uncertainty of the arrival time readings. Of the 49 events in the cluster, 46 have a formal location accuracy of better than 5 km (longest semi-axis). Given that depths were held fixed and could be in error by 5–10 km, and also that we used arrival time data from somewhat greater epicentral distances than optimal for locating the hypocentroid, the epicentral location uncertainties are likely underestimated by perhaps 1–2 km.

Berberian (1979) places the epicentres of the 1973.05.11 and 1974.06.17 earthquakes (event Nos. 2 and 3 in Table 1) at the villages of Shahzadeh Ali and Fosha (labelled in Fig. 2). These macroseismic epicentres are far from our instrumental locations (by up to 20 km in the case of the 1973 Shahzadeh Ali event). Unfortunately we are unable to reconcile the instrumental relocations in Table 1 with the macroseismic locations. The majority of the readings that we used in the HDC analysis for these two events are well fit, with few outliers, and no evidence of anomalies in the dataset that could produce a biased location.

An alternative possibility for the mismatch in locations is the overall calibration of the cluster. To test for this, we performed an 'indirect' calibration, forcing the cluster to shift so that the two macroseismic locations are satisfied. The best fit is achieved if the entire cluster is shifted about 17 km to the NNW, which puts the 1974.06.17 event ~4.5 km NW of Fosha village, and the 1973.05.11 event ~4.5 km SE of Shahzadeh Ali. However, calibrating the cluster location is this way introduces large residuals (4–5 s) in some of the local distance readings that are matched reasonably well with our original calibration, and it introduces a bimodal distribution on the near-regional Pn data, such that stations to the NW have large positive residuals. With our original calibration, all the near regional Pn data are fit pretty well with a common travel-time model. Overall, our analysis of the readings used to locate the 1973 and 1974 events suggests that the instrumental epicentres are unlikely to be biased by the amounts required to satisfy the macroseismic data.

4.2. The 1978 Tabas earthquake

The relocated epicentre of the 1978 Tabas main-shock is at 33.205°N 57.424°E, placing it close to the southern end of the observed surface ruptures and indicating a unilateral northward rupture propagation. Analysis of strong-motion records by Shoja-Taheri and Anderson (1988), and Sarkar et al. (2004), indicate the presence of at least four, and probably more, discrete sub-events in the main-shock. Although

Fig. 3. (A) ASTER satellite image of the Sardar fold segment. (B) Annotated version of 'A'. The abandoned fan surface (F1) of the Sardar River is highlighted in light grey (gold in online version), and the remnants of older fan surfaces isolated within it are shown in darker shades of grey (orange and red in online version). Exposures of underlying Neogene marls are marked in black (green in online version). The mapping of Neogene and Quaternary outcrops is from our own interpretation of the satellite imagery. A topographic profile across the fold was measured along the dotted line. Structural and bedding measurements through the fold were taken along the Sardar River canyon. The topographic profile and structural measurements are projected onto the line a–b in later figures.

Please cite this article as: Walker, R.T., et al., Co-seismic, geomorphic, and geologic fold growth associated with the 1978 Tabas-e-Golshan earthquake fault in eastern Iran, Geomorphology (2013), http://dx.doi.org/10.1016/j.geomorph.2013.02.016

Table 1
Calibrated epicentres of earthquakes in the study region determined with the methods described in Section 4. A1 and A2 are the azimuths in degrees, clockwise from north, of the semi-axes of the 90% confidence ellipse for the epicentre. L1 and L2 represent the lengths of the corresponding semi-axes in km. Area is the area in km^2 of the 90% confidence ellipse. Magnitudes of older events are assigned from the ISC bulletin, and for more recent events are M_L values from the Iranian seismological networks. Those events for which body-waveform or CMT solutions are available (Table 1) are shown in bold.

No.	Date	Time (GMT)	Latitude	Longitude	Depth	Mag	A1	L1	A2	L2	Area
1	1973.05.05	06.12:31.68	33.304	57.452	12	4.5	70	3.3	160	5.0	52
2	1973.05.11	13.52:24.86	33.286	57.496	8	5.1	75	2.1	165	3.6	23
3	1974.06.17	07.22:44.85	33.636	57.039	12	4.7	77	2.3	167	4.1	30
4	**1978.09.16**	**15.35:52.31**	**33.205**	**57.424**	**12**	**6.4**	**82**	**2.0**	**172**	**3.6**	**22**
5	1978.09.17	07.35:45.87	33.056	57.025	12	4.6	71	2.3	161	3.9	29
6	1978.09.17	08.17:20.72	33.508	57.072	12	4.9	80	2.2	170	3.9	27
7	1978.09.18	04.49:59.41	33.405	57.461	12	4.7	21	5.0	111	5.3	82
8	1978.09.22	18.53:02.76	33.131	56.865	12	4.4	80	2.0	170	3.7	23
9	1978.10.09	16.04:38.91	33.251	57.346	18	4.6	276	3.0	6	4.4	42
10	1978.10.12	15.01:38.69	33.254	57.445	11.3	4.9	271	2.4	1	4.2	32
11	1978.12.06	17.18:10.44	33.214	57.121	12	5.3	76	2.5	166	3.8	30
12	1978.12.06	20.38:08.31	33.099	57.167	22	4.7	71	4.3	161	4.6	62
13	1979.01.17	03.29:45.82	33.616	57.068	12	5.1	83	2.2	173	3.6	24
14	**1979.02.13**	**10.36:13.51**	**33.19**	**57.467**	**18**	**5.4**	**79**	**1.9**	**169**	**3.4**	**20**
15	1979.05.27	06.43:14.96	33.161	57.358	12	4.6	83	2.3	173	4.0	29
16	1979.07.05	04.46:07.59	33.401	57.078	12	4.5	74	2.3	164	4.4	31
17	1979.12.02	06.10:45.6	33.562	57.12	12	4.7	74	2.5	164	4.0	31
18	1979.12.20	00.33:46.74	33.159	57.486	12	4.5	319	5.4	49	6.9	116
19	**1980.01.12**	**15.31:37.89**	**33.472**	**57.22**	**12**	**5.3**	**79**	**1.8**	**169**	**3.3**	**19**
20	1987.07.20	16.47:44.72	33.731	57.049	16	5	79	1.9	169	3.4	20
21	1987.08.30	05.57:50.66	33.343	57.174	20	4.7	80	1.9	170	3.5	21
22	1990.03.25	00.01:07.29	33.613	57.057	20	4.8	81	2.0	171	3.8	24
23	1990.10.15	19.06:48.72	33.616	56.888	12	4.9	81	1.8	171	3.5	20
24	1991.10.23	20.45:03.87	33.028	57.444	12	4.6	282	2.3	12	5.4	40
25	1992.09.06	08.42:05.36	33.688	56.966	20	4.7	82	1.8	172	3.6	21
26	1998.03.26	20.08:16.35	33.931	57.05	12	3.9	277	2.2	7	5.6	39
27	1998.03.27	01.21:20.48	33.058	57.003	12	4.5	277	2.4	7	5.4	40
28	2000.12.23	20.42:38.14	33.245	57.267	12	3.1	18	3.8	108	5.0	60
29	2001.09.01	10.45:52.89	33.196	57.339	12	3.9	70	2.8	160	4.0	35
30	2001.09.02	02.48:52.91	33.212	57.285	12	3.7	356	4.8	86	7.5	113
31	2001.09.24	16.53:14.27	33.293	57.513	12	4.2	76	1.8	166	3.4	19
32	2002.04.16	03.34:16.66	33.226	56.933	12	3.7	24	4.3	114	5.5	73
33	2002.08.16	07.14:29.92	33.398	57.238	12	3.8	72	2.3	162	4.2	30
34	2003.02.10	04.39:03.4	33.621	56.978	12	3.2	72	3.0	162	4.0	37
35	2003.05.22	11.09:30.3	33.111	57.474	12	4.2	71	2.2	161	3.9	27
36	2003.10.21	14.45:30.56	33.28	57.37	12	3.6	54	2.6	144	4.6	38
37	2005.03.28	15.33:19.21	33.423	57.163	12	0	71	2.2	161	3.6	25
38	2005.07.10	13.47:19.55	33.728	56.787	12	0	74	2.2	164	4.0	28
39	2006.08.16	09.09:05.26	33.373	56.898	12	4.3	74	1.8	164	3.4	19
40	2006.08.19	00.26:57.46	33.351	56.869	12	3.6	73	1.7	163	3.3	17
41	2006.09.24	10.30:07.19	33.681	56.891	12	3.7	73	1.7	163	3.2	17
42	2007.01.07	15.32:18.4	33.984	56.662	12	4.5	74	1.8	164	3.4	19
43	2007.01.07	18.25:15.99	33.993	56.64	12	3.4	76	2.1	166	3.6	23
44	2007.04.16	01.22:56.65	33.927	56.677	12	3.6	73	1.9	163	3.5	21
45	2008.01.19	21.41:24.77	33.268	57.353	12	4.4	72	1.8	162	3.4	19
46	2008.08.24	14.52:47.25	33.011	56.89	12	3.6	73	2.0	163	3.5	22
47	2010.05.18	03.59:36.84	33.667	56.862	12	3.8	73	1.9	163	3.5	21
48	2010.10.06	23.47:57.44	33.379	57.184	12	4.2	74	1.7	164	3.3	18
49	2010.10.27	18.53:53.65	33.242	57.398	12	3.9	73	1.8	163	3.4	19

there are no constraints on the locations of individual sub-events, it is likely that they correspond to segmentation of the fault, as also indicated in the discrete fold segments visible in the geomorphology and in the discontinuous surface rupturing (Berberian, 1979).

The source parameters of the 1978 main-shock indicate slip on a north–south fault dipping ~16°E and with a slip-vector azimuth of 019° indicative of thrusting with a right-lateral component (e.g. Walker et al., 2003). Similar source parameters were obtained for the 1979 and 1980 shocks, though with slightly steeper dips (28° and 20° respectively), and with slip-vector azimuths of 028° and 029°. The 1978 earthquake had a centroid depth of 9 km, and the 1979 and 1980 events had centroid depths of 11 km and 14 km respectively.

Walker et al. (2003) calculated, from scaling relationships, that the average slip at depth would be ~3.3 m. Some slip on the main thrust fault may have reached the surface, particularly along western margin of the folds close to Khalilabad and south of Kurit (Fig. 2; Berberian, 1979). However, as the maximum measured thrust displacement at the surface was only 35 cm (Berberian, 1979), the major part of the primary rupture is likely to have been blind. Much of the surface deformation observed following the earthquake, which included widely distributed bedding-plane slip within the folds as well as steeply dipping to vertical faults, is likely to result from co-seismic fold growth (e.g. Walker et al., 2003). A right-lateral component was noted on several of the distributed faults within the Tabas folds (Berberian, 1979).

Much of the seismicity in the Tabas region, including the 1979.02.13 earthquake (event No. 14; Mw 5.6), is concentrated immediately north and west of the 1978 main-shock. Seismicity extends NNW from the 1978 main-shock in the hanging-wall of the fault segments that are known, or inferred, to have ruptured in the 1978 earthquake. The 1980.01.12 earthquake (event No. 19; Mw 6.0) occurred within this zone with a similar focal mechanism to the 1978 main-shock. An event in 1990.03.25 with a focal mechanism indicative of NNW–SSE left-lateral faulting or ENE–WSW right-lateral faulting may by caused

Please cite this article as: Walker, R.T., et al., Co-seismic, geomorphic, and geologic fold growth associated with the 1978 Tabas-e-Golshan earthquake fault in eastern Iran, Geomorphology (2013), http://dx.doi.org/10.1016/j.geomorph.2013.02.016

by tear faulting between individual thrust fault segments. We note that apart from the concentration of events in the south, and from one isolated event in the far north (event No. 26), all events are located west of the Shotori range-front.

Two surprising features of the seismicity shown in Fig. 2 are the relatively large amounts of seismicity within the Tabas playa lake. This seismicity occurs in two zones; a southern zone north of the Cheshmeh Rostam Fault (which did not rupture at the surface in the 1978 earthquake), and a northern zone situated northwest of Tabas town. The northern zone includes a relatively large event (Mw 5.1) in 1990 (event No. 23). Seismicity within the playa may indicate that blind faulting associated with the Tabas system extends west of the visible manifestations of folding, though we have no means of verifying this speculation.

Aftershock locations from a local seismometer deployment by Berberian (1982) show a broadly similar distribution to our relocated teleseismic events, with most of the aftershocks located in the hanging-wall of the Tabas Faults, scattered seismicity in the Tabas playa, and very little activity beneath the Shotori Mountains. The aftershocks of Berberian (1982) show a concentration in depth at ~10 km (e.g. Fig. 4 of Walker et al., 2003).

5. A structural transect through the Sardar fold

Examination of the cumulative deformation and folding recorded in the geology of the Tabas region has the potential to provide additional constraints on the source of the 1978 Tabas earthquake. Fig. 2 shows the major segments of the Tabas blind thrust system. Along most of the length of the system there are several parallel folds, each of which is likely to be underlain by faults, and each of which will contribute to the overall rate of shortening. North of Tabas town, however, only one main band of folding is apparent in the geomorphology. A small remnant of incised alluvial fan deposits, trending NNW–SSE between the Sardar fold and Tabas town (Fig. 3), might represent the presence of an additional active fault in the footwall of the Sardar blind thrust. However, given that deformation of the alluvial surface caused by this additional fault is not visible apart from a short ~1 km section, it is likely that any folding across this structure will be minor in comparison to that across the Sardar fold (e.g. Daeron et al., 2007).

The deep incision of the Sardar River allows us to produce a detailed section, with almost continuous fresh exposure, through a fold that is known to have deformed during the 1978 Tabas earthquake (e.g. Berberian et al., 1979). In addition to learning about the long-term development of the Sardar fold segment, our structural observations have the potential to provide additional constraints on the 1978 earthquake source. We noted lithological changes, recorded structural information, and took numerous bedding orientations along the canyon (Fig. 4A). A cross-section constructed from our field measurements is shown in Fig. 4B. Field photographs showing the important structures are shown in Figs. 5 and 6.

In the westernmost part of the section, where the Sardar River has incised only ~5 m into the surface of the F1 alluvial fan surface, the exposed gravels dip <5° to the west. The youngest gravel deposit, corresponding to the incised Sardar fan surface visible on satellite imagery, is visible as a 2–4 m thick grey-coloured gravel unit conformably overlying older, orange-stained, gravel units. Observable tilting of older gravel units is first observed at ~57°02′10″E (~3200 m along profile) where the uppermost alluvial units lie unconformably on older gravel units dipping ~10°W. A rapid increase in dip from 10°W to 40°W, along with truncation of successively older units, is noted at ~57°02′19″E (Fig. 6A; 3800 m along profile). The uppermost alluvial unit, with a thickness of ~2 m, unconformably overlies the tilted units. This zone of abrupt tilting of gravel deposits is visible at the surface as a ramp in the topography (Fig. 5).

Continuing westwards along the profile, successively older gravel units, all dipping ~40°W, are exposed in the deepening canyon walls. A lithological boundary is seen at ~57°02′27″E (~4000 m along profile), where the gravel units grade downwards into fine-grained, and light-coloured, marly sandstones. The upper marl units contain matrix-supported gravel horizons. The sediments rapidly fine downwards into uniformly fine-grained, presumably lacustrine, deposits. Rare gravel horizons are, however, still present within the lakebed exposures.

The appearance of finer-grained basin sediments is accompanied by the occurrence of widespread faulting along bedding planes (Fig. 6B–C). Co-seismic bedding-plane slip, with displacements of ~10 cm on many tens of bedding planes, was observed widely following the 1978 earthquake (e.g. Berberian, 1979) and is thought to represent co-seismic flexural slip folding above the tip of a blind thrust fault (e.g. Walker et al., 2003). The uppermost gravel units, which unconformably overlie the tilted marl units, thicken by several metres upstream of zones of bedding slip, indicating that prior to deposition of the most recent alluvial units, east-facing scarps with heights of several metres had developed due to repeated bedding-slip events (Fig. 6B). Slickensides measured on exposed bedding-planes indicate slip-vector azimuths of ~25° (Fig. 6C). The measured slip-vector azimuths, which are oblique to the WSW–ENE dip of the bedding, indicate a large component of right-lateral strike–slip distributed through the forelimb of the fold.

An abrupt increase in dip from ~40°W to 60°W occurs between 57°02′36″E and 57°02′38″E. The steepening dip of beds is accompanied by a zone of intense bedding-slip, and of faults dipping 70–80°W that cut across bedding, and have slip-vector azimuths of 330–350° that indicate almost pure strike–slip displacement across them (Fig. 6D).

The oldest exposed basin sediments, which are red in colour and heavily deformed, are exposed over a distance of ~50 m in the core of the anticline near 57°02′59″E (~4600 m along profile). The canyon widens in the fold axis, perhaps indicating that the red marls are less resistant to fluvial erosion than overlying units.

The eastern limb of the fold is much less deformed than the western limb, with a maximum bedding dip of ~20°E, and an absence of widespread bedding-plane slip. Minor faults do, however, occur within the eastern fold limb. These faults are mostly thrusts that cut across bedding with dips of 25–45°E (e.g. Fig. 6E). The slip-vector azimuths measured from these faults, which range from 60° to 70°, indicate almost pure shortening.

A syncline axis, with folding accommodated by bedding-slip and by movement on minor steep-dipping reverse faults, was observed near ~57°03′24″E (~5500 m along profile). The F1 gravels, which unconformably overlie the folded marls, thicken at the syncline axis. Bedding dips of ~15–20°E are observed, once again, by 57°03′44″E. At 57°03′51″E there is an abrupt, though conformable, transition from marly sandstone to conglomerate (e.g. Fig. 6F). Within the tilted conglomerate exposed in the eastern limb of the fold, the Sardar River channel narrows to a width of only ~2–3 m, and our structural measurements along this section of the profile are instead taken from an exposure at the top of the canyon and accessible from the road-side. The dip of gravel beds decreases from 20°E to <5°E over a distance of just a few hundred metres at 57°03′34″E. East of this location the canyon exposes a uniform sequence of coarse gravels with no measureable dip.

In summary, the fold is asymmetric, with a steep western forelimb with dips of up to ~60°, and a gentle eastern back-limb with dips of ~20°. From this asymmetry, and from the observation that the forelimb of the fold is not truncated by a main thrust fault, we interpret the structure as a fault-propagation fold overlying a thrust dipping ~20° to the east. This inferred structure is consistent with the common occurrence of bedding-plane slip only in the forelimb, as the back-limb of the fold represents lateral

Please cite this article as: Walker, R.T., et al., Co-seismic, geomorphic, and geologic fold growth associated with the 1978 Tabas-e-Golshan earthquake fault in eastern Iran, Geomorphology (2013), http://dx.doi.org/10.1016/j.geomorph.2013.02.016

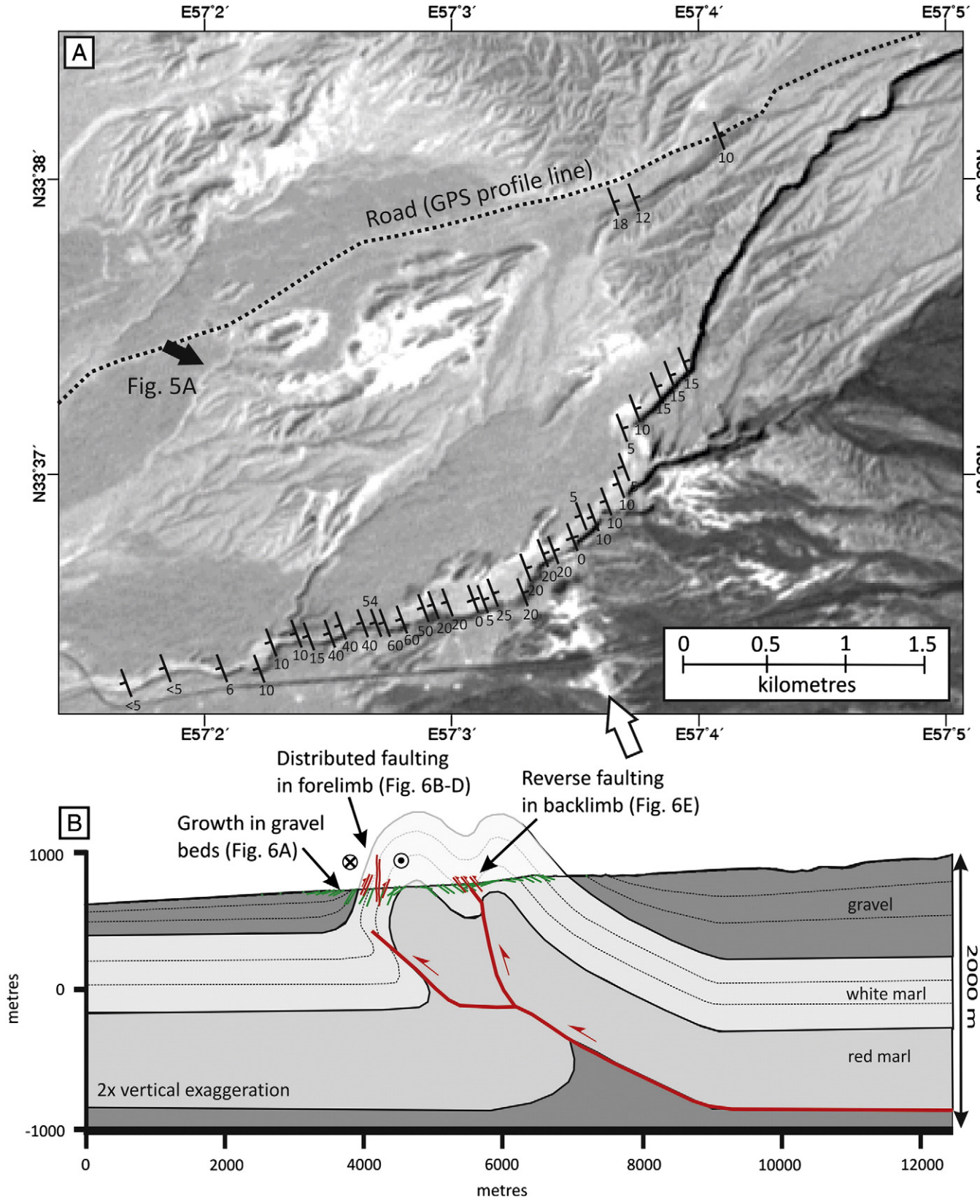

Fig. 4. (A) Bedding orientations measured from exposures in the Sardar River canyon and by the roadside. The magnitudes of dip are labelled and the short ticks indicate dip direction. The white arrow points along a west-facing scarp along strike of a zone of reverse faulting observed in the back-limb of the Sardar canyon fold. (B) Cross-section through the Sardar fold based on measurements from the Sardar River canyon (projected onto profile line a–b in Fig. 3). Black ticks (green in online version) represent dip measurements. Thick black lines (red in online version) are faults. The underlying thrust flattens out at a depth of ~2 km. Deformation within the back-limb is manifest as secondary folding and a zone of east-dipping reverse faults. Right-lateral strike–slip on the underlying thrust is accommodated by distributed faulting within the forelimb of the fold. The topography in this section comes from the SRTM dataset.

Please cite this article as: Walker, R.T., et al., Co-seismic, geomorphic, and geologic fold growth associated with the 1978 Tabas-e-Golshan earthquake fault in eastern Iran, Geomorphology (2013), http://dx.doi.org/10.1016/j.geomorph.2013.02.016

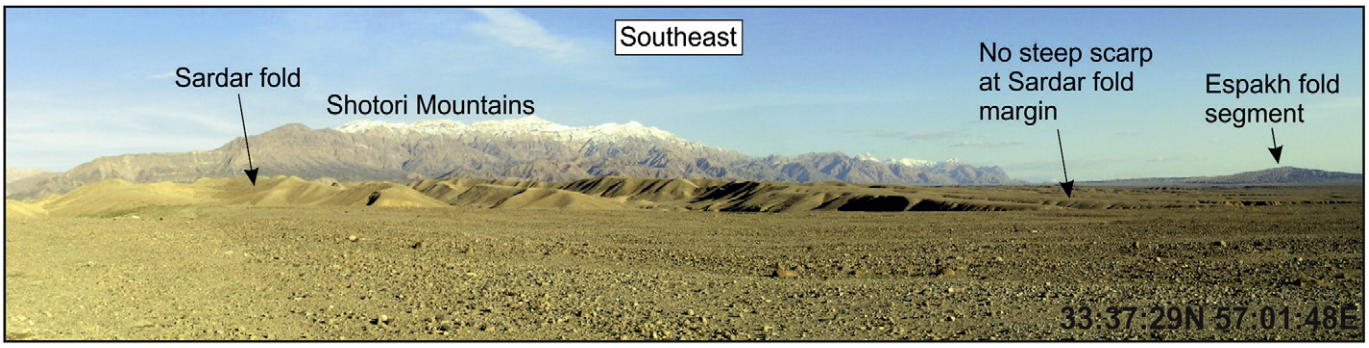

Fig. 5. Photograph looking southeast at the western flank of the Sardar anticline. No steep scarp is visible, and the fan surfaces (F1 and older) are instead gently warped as they cross the margin of the fold. The warping in the topography visible in this photograph corresponds with a zone of abrupt tilting of older gravel beds exposed in the Sardar canyon (Fig. 6A). See Fig. 4A for photograph location.

transport of sediments in the hanging-wall without continued limb rotation.

The presence of a secondary fold axis east of the main anticline axis, and the widespread presence of steep faults cutting through the exposed sediments, shows that deformation occurs within the hanging-wall of the basal fault. We interpret the hanging-wall deformation as a combination of folding above a slight ramp in the basal thrust and a steep reverse fault splay originating at this bend in the main fault. We note there is a clear west-facing scarp visible in satellite imagery south of the Sardar River exposures and along strike of the zone of hanging-wall folding and faulting (Fig. 4A).

6. Late Quaternary deformation of the Sardar alluvial fan surface

Deposits of the F1 Sardar alluvial fan extend over a distance of ~20 km from the Shotori Mountain range-front to the edge of the Tabas playa (Fig. 3). The fan surface is traced continuously across the Sardar anticline, and is preserved without interruption in three narrow channels. There is no visible evidence for displacement of the F1 fan surface as it crosses the Shotori range-front (Walker et al., 2003).

To provide an additional constraint on the structure of the Sardar blind thrust we produced a topographic profile along the surface of the F1 alluvial fan surface, perpendicular to the fold axis. With the rover antenna mounted on our vehicle, the profile was measured with differential GPS along a dirt road on the F1 fan surface (Fig. 3). The GPS measurements were then projected onto a single profile line (profile A–B in Fig. 3) to produce a topographic section perpendicular to the fold axis. The topographic section is shown in Fig. 7A. As the topography is dominated by the ~2° depositional slope of the fan surface itself, we also present an uplift profile, in which we have subtracted a linear slope with a gradient of 0.259 from the topographic profile (Fig. 7B). This linear slope fits the topographic data from the westernmost and easternmost parts of the topographic profile and we assume that it approximates the original, undeformed, fan surface.

The uplift profile (Fig. 7B) indicates that warping of the F1 fan surface occurs over a distance of ~6 km. The shape of the uplift is consistent with what is expected from anticlinal folding above an east-dipping thrust with a short, steep, forelimb in the west and a gentle back-limb in the east. The broad topographic variations are superimposed on short-wavelength highs and lows that are likely to be caused by either man-made features or by natural erosion (the low at ~5000 m along the profile may correspond to the road following a slight stream incision in the F1 surface and the spike, at ~8000 m from the western end of the profile, is likely to correspond to the road climbing onto an older fan surface for a short distance). In Fig. 7B, we have sketched two profiles to show the uplift expected with a single anticline axis and with two axes. The measured topography is suggestive of folding on two axes. The maximum uplift of ~9 m in the topographic profile is located close to (actually a little east of) the eastern of the two anticline axes seen in the geology. Approximately 4 m of this uplift occurs above the western fold axis, and the remaining ~5 m above the eastern axis.

An important point to note is that although the F1 alluvial fan surface is uplifted across the Sardar fold by only ~9 m, it is incised by a canyon up to 100 m deep (e.g. Walker et al., 2003). The major part of the incision of the Sardar River hence appears to be unrelated to tectonic uplift, and is instead likely to be a response to environmental changes since abandonment of the fan surface (e.g. Walker and Fattahi, 2011). We return to the implications of this observation in Section 8.2.

7. Estimate of the late Quaternary slip-rate of the Tabas and Nayband faults

7.1. Dating the Sardar alluvial fan abandonment

To provide an estimate of the slip-rate on the Tabas thrust faults we must first determine the age of the F1 fan surface. We excavated a single 2-m-deep pit into the fan surface at 33°39′12.9″N 57°05′54.4″E (Fig. 8). The site was selected for its planar surface and the absence of obvious disturbance by small distributary channels on the fan surface. The exposed alluvial deposits are primarily composed of limestone with rare chert clasts. The material is very coarse, with clasts typically of several centimetres diameter and occasional boulders of >15 cm diameter, set in a sand/silt matrix. No predominantly fine-grained horizons were found in either the sample pit or in accessible natural exposures in the Sardar canyon.

To date the surface we combined optically-stimulated luminescence (OSL) on quartz grains, Infra-red stimulated luminescence (IRSL) on K-feldspar, and ^{36}Cl cosmogenic radionucleide exposure (CRE) concentrations in a vertical profile from the surface to 2 m depth. As luminescence dating provides the date when buried sediment was last exposed to sunlight, and CRE dating determines the length of time that an alluvial surface has been exposed to cosmic radiation at or near the Earth's surface, the two dating methods are complementary and, by combining them, we hope to generate firm constraints on age.

7.1.1. Luminescence dating

A single OSL sample was collected at a depth of ~60 cm below the surface from the wall of the sample pit. To prevent light exposure whilst the sample was collected the pit was covered by layers of black plastic and canvas. Care was taken to remove the outer light-exposed wall of the pit before the sample was collected. A portion of loose sediment was then scraped from the wall, sieved to

Please cite this article as: Walker, R.T., et al., Co-seismic, geomorphic, and geologic fold growth associated with the 1978 Tabas-e-Golshan earthquake fault in eastern Iran, Geomorphology (2013), http://dx.doi.org/10.1016/j.geomorph.2013.02.016

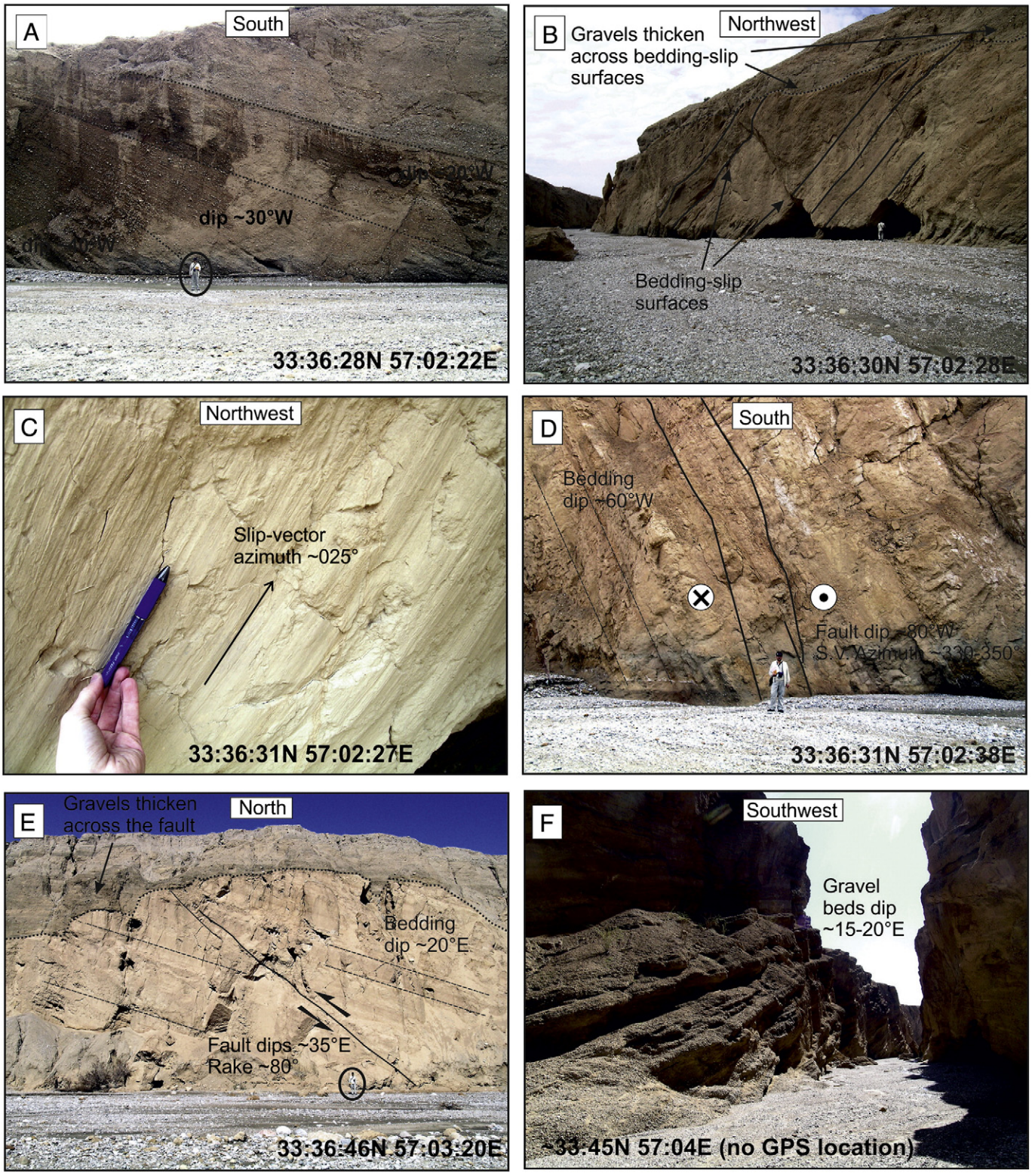

Fig. 6. Field photographs showing some of the major structures observed within the Sardar canyon. See Fig. 4B for locations along the structural profile. (A) Zone of abrupt tilting in gravel beds exposed in the Sardar canyon. (B) Slip surfaces along tilted bedding in marl deposits. Gravels corresponding to the deposition of the F1 fan lie unconformably over the tilted marls. The gravels thicken on the downthrown side of the bedding-slip surfaces. (C) Striations on the bedding-slip surfaces. (D) A zone of steep, and almost pure strike–slip faulting, cutting through marl deposits dipping 60°W. (E) Reverse faulting cutting through the eastern limb of the Sardar fold. The overlying F1 gravels thicken across the fault. (F) View within the eastern limb of the fold showing constant 15–20°E dip within beds.

remove large (>2 mm) grains within the deposit, and then stored in an opaque black plastic bag. The sample was wrapped in additional layers of black plastic and then sealed with thick tape. This method of sample collection was adopted as the sediment was too coarse to insert a tube and not cohesive enough to allow the extraction of a large intact block of sediment.

Please cite this article as: Walker, R.T., et al., Co-seismic, geomorphic, and geologic fold growth associated with the 1978 Tabas-e-Golshan earthquake fault in eastern Iran, Geomorphology (2013), http://dx.doi.org/10.1016/j.geomorph.2013.02.016

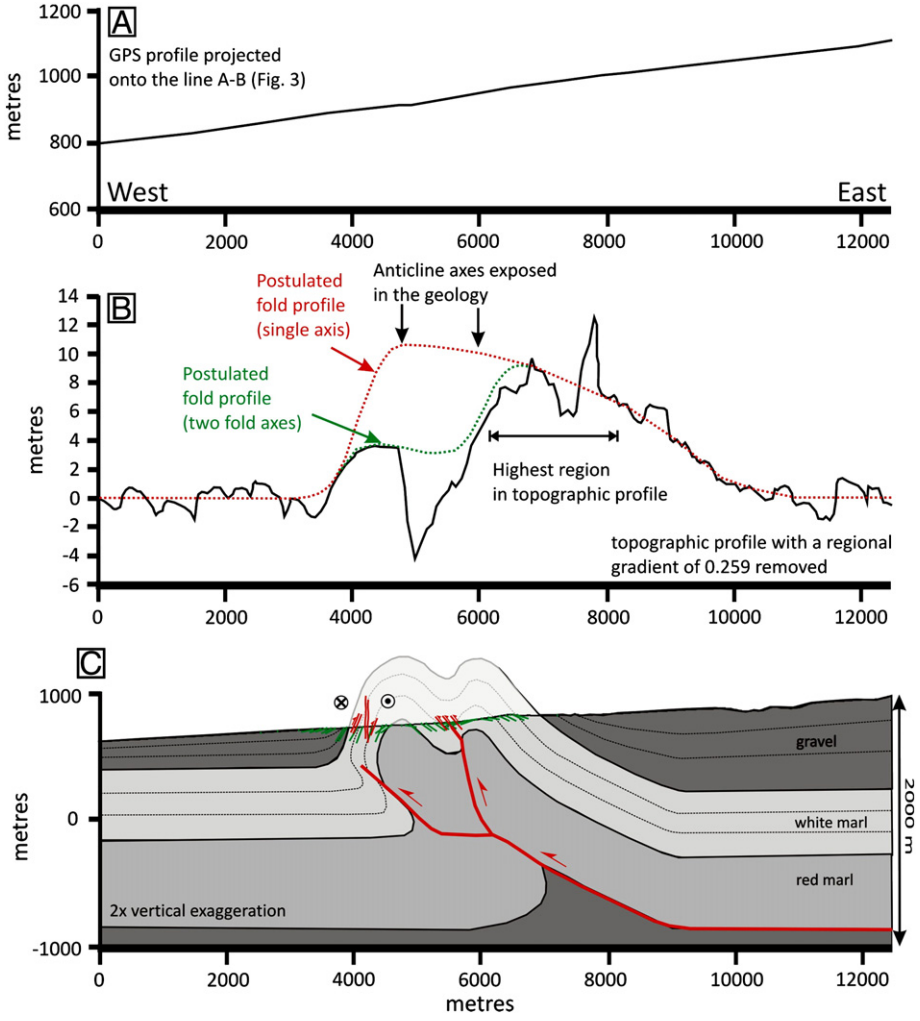

Fig. 7. (A) Topographic profile along the F1 fan surface. The profile has been projected onto profile A–B in Fig. 3. (B) The profile in 'A' with a regional gradient of 0.259 removed in order to show warping of the surface. Uplift and deformation of the F1 surface begins ~3500 m from the western end of the profile, at a similar location to the abrupt tilting observed in gravel units (Fig. 6B), though the peak uplift is observed ~7000 m along the profile. The overall uplift is consistent with warping above two fold axes as also observed in the geology. (C) Structural cross-section shown at the same horizontal scale as the topographic profile.

The sample was processed under subdued red light. A portion of the sample was wet-sieved to separate coarse grain quartz and feldspar (90–250 μm and 250–500 μm) size fractions and immersed for two weeks in 1 N HCl to remove carbonate, followed by two days immersion in H_2O_2 to remove organic material. Heavy minerals (density > 2.72 g/cm^{-3}) were removed from the treated sample fraction (90–250 μm size fractions) by heavy liquid (sodium polytungstate) separations. A further heavy liquid separation (density = 2.58 g/cm^{-3}) separated quartz and potassium feldspar (density < 2.58 g/cm^{-3}). The quartz was etched by 48% HF for 60 min. At each stage of the separation procedures, samples were generously rinsed with distilled water. For the single aliquot analyses, the quartz and feldspar separates were mounted as monolayers (approximately 5 mg/per disc) on 10 mm diameter aluminium discs using a silicon spray as an adhesive. The instruments and measurements are the same as those used by Fattahi et al. (2006).

The equivalent dose (De) was obtained using the SAR (Single Aliquot Regeneration) method (e.g. Murray and Wintle, 2000) for both quartz and feldspar. The preheat and cut-heat treatments were at 260 °C and 220 °C for 10 s for quartz measurements. IRSL and OSL were measured for 100 s, respectively at 125 °C sample temperature. Unfortunately, according to our experiments, quartz separates of these samples were not very suitable for luminescence dating because after heavy liquid separation and acid treatment there was a reasonable IRSL signal. Therefore, for De measurement of quartz, we stimulated the sample using IR, immediately after both preheat and cut heat, for 60 s and then measured OSL signal. The net initial luminescence signal was used for natural, regenerated and test dose measurements. The De was determined by interpolation and the sensitivity was corrected by dividing Lx by Tx. No aliquot produced significant recuperation signals (~2% natural). Most aliquots produced a recycling ratio between 0.9 and 1.09. Those that did not were not used in the De calculation.

Eighteen aliquots were prepared from both the feldspar and quartz separates. For each aliquot, after measurement of the natural dose, a dose–response curve was constructed from five dose points including three regenerative doses, and a zero dose. A replicate measurement of the lowest regenerative dose was carried out at the end of each SAR cycle.

Fig. 9 shows the dose distribution for the potassium feldspar grains (left column) and quartz grains (right column). Table 3 shows the ages calculated from the equivalent dose measurements using weighted mean, minimum De, and central age models. No fading test was performed for the feldspar sample. Weighted mean ages of 27.3 ± 8.0 ka (quartz OSL) and 19.0 ± 3.4 ka (feldspar IRSL) are

Please cite this article as: Walker, R.T., et al., Co-seismic, geomorphic, and geologic fold growth associated with the 1978 Tabas-e-Golshan earthquake fault in eastern Iran, Geomorphology (2013), http://dx.doi.org/10.1016/j.geomorph.2013.02.016

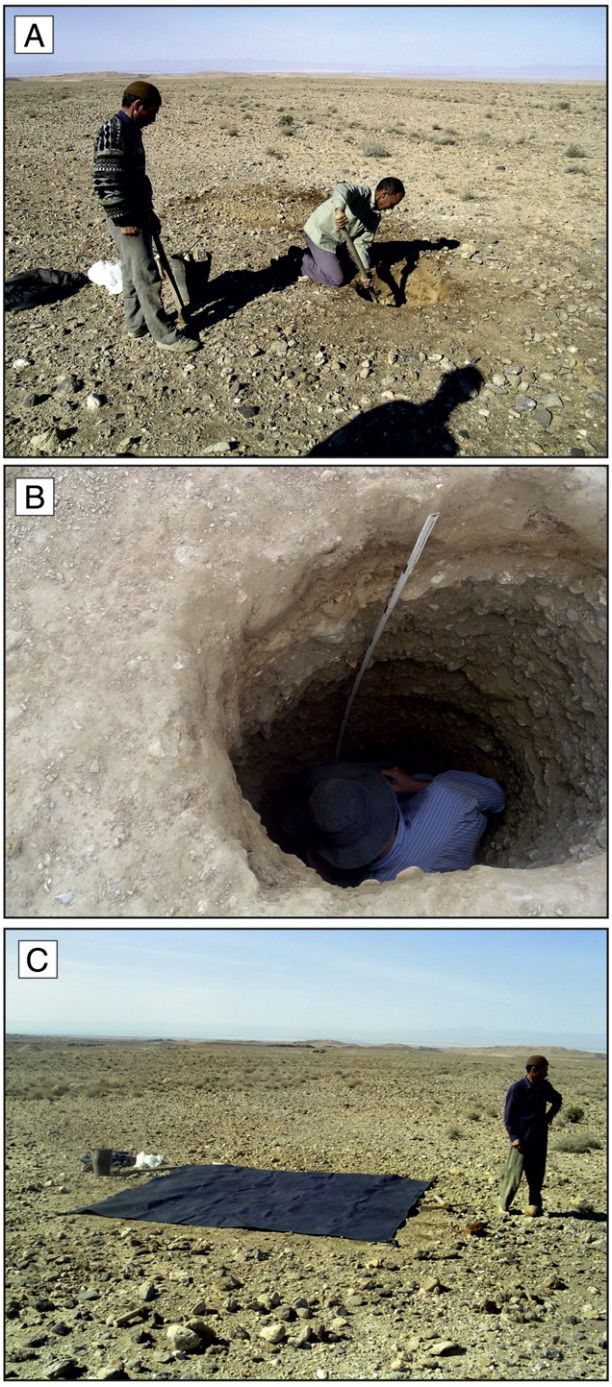

Fig. 8. Field photographs showing the location and surroundings of the sample pit at 33°39′12.9″N 57°05′54.4″E. (A) Excavation of the pit. (B) Collecting amalgamated samples of clasts from the pit walls for a depth profile of cosmogenic ^{36}Cl. (C) Collection of sediment for luminescence dating was performed whilst covered by layers of plastic and canvas.

calculated from the De distributions. These weighted mean ages are similar to ages calculated using a central age model (Galbraith et al., 1999; Table 3).

The alluvial sediments in the Sardar fan are typically coarse-grained and are likely to have been deposited rapidly and in high-energy conditions. The equivalent dose (De) measurements for both the quartz OSL and feldspar IRSL show considerable scattering between aliquots and suggests that the luminescence signal in many of the grains was only partially reset prior to deposition (Fig. 9). The luminescence responses of quartz and feldspar grains in Iran are often extremely dim such that single-grain analyses, which are often preferable when dealing with alluvial sediments (e.g. Duller, 2008), are not typically viable. As the response from individual aliquots is so dim, the observed signal is likely to originate from just a few grains in each, such that the De measured from each aliquot in the dose distribution diagrams may approximate to measurements from single grains (Le Dortz et al., 2011).

Assuming that the scatter in the De measurements from the Sardar fan arises from incomplete resetting of mineral grains immediately prior to deposition, the minimum measured value of De is most likely to be closest to the real age of deposition, though even the minimum De measurement may retain some inherited signal. Using the minimum De yields ages of 12.5 ± 1.3 ka (quartz OSL) and 15.2 ± 1.2 ka (feldspar IRSL). Several studies around eastern Iran have dated the end of the most recent period of alluvial fan deposition to be in the range of 10 ± 2 ka, with the younger end of this range supported by several of the most well constrained studies (e.g. Le Dortz et al., 2011; Walker and Fattahi, 2011). Therefore, although our mimimum De age falls within the 10 ± 2 ka age range that is often found within eastern Iran, the actual abandonment age of the Sardar fan F1 age may be younger than the 12.5 ± 1.3 ka obtained from the minimum De method, and may be as young as 8 ka.

7.1.2. Cosmogenic ^{36}Cl exposure dating

We collected ten samples of amalgamated centimetric clasts of limestone from the surface down to a depth of 1.8 m. Each amalgamated sample contained several tens of clasts collected over a depth interval of 5 cm. The samples were crushed, sieved to 125–250 μm and leached in hot 2 M HNO_3 to remove meteoric ^{36}Cl contamination. Each sample was then split into two fractions: c. 2 g for elemental analysis and c. 20 g for analysis of ^{36}Cl with accelerator mass spectrometry (AMS). Results are shown in Table 4. Chlorine was extracted and purified to produce AgCl for AMS analysis according to the procedures described in Vincent et al. (2010). AMS measurements were performed according to Maden et al. (2007).

The ^{36}Cl CRE data are shown in Table 4 and in Fig. 10. We used the model of Schimmelpfennig et al. (2009) to model an age from the concentrations. We used the production rate of Stone et al. (1996). Local scaling factors were calculated from the latitude and elevation using the scheme of Stone (2000) According to this model, the ^{36}Cl in the Tabas samples is mainly produced by spallation reactions of Ca (~73%), capture of thermal neutrons by ^{35}Cl (~12%) and direct capture of slow negative muons by Ca (~11%). As the concentrations of Ca and Cl are homogeneous along the depth profile (Table 4), a mean composition of the samples was used. Current inheritance ($N_{inher.}$), exposure age (t), erosion rate (ε) and density (ρ) were considered as free parameters to fit the model to the dataset. Hence, a model with four free parameters was used to fit 10 ^{36}Cl concentrations, implying 6 degrees of freedom (DOF). Monte Carlo simulations were used to find the values that fit the data within 1σ confidence level (Table 5). Simulations yielded best fits with a χ^2 of ~30. Thus, a maximum χ^2 value of ~33 was considered (68.27% of possible χ^2 values, see Rodés et al., 2011). Best fits and extreme results were checked using χ^2 minimisation.

The model results shown in Table 5 allow us to determine a current ^{36}Cl inheritance of 1.1 ± 0.1 million ^{36}Cl atoms per gramme. If we consider a deposition age between 8 and 14 ka (using a-priori age constraints from our minimum De OSL age of 12.5 ± 1.3 ka, and acknowledging that the fan abandonment age may be younger than implied by the minimum De estimate, as described in the previous section), the model only fits the CRE data for erosion rates of >340 mm/ka at the sampling site. The range of acceptable model results is shown as a grey shaded area in Fig. 10. Moreover, considering a deposition age of ~10 ka, current ^{36}Cl inheritance implies an apparent exhumation rate of ~110 mm/ka in the source area of the Sardar alluvial fan sediments within the Shotori Mountains.

Please cite this article as: Walker, R.T., et al., Co-seismic, geomorphic, and geologic fold growth associated with the 1978 Tabas-e-Golshan earthquake fault in eastern Iran, Geomorphology (2013), http://dx.doi.org/10.1016/j.geomorph.2013.02.016

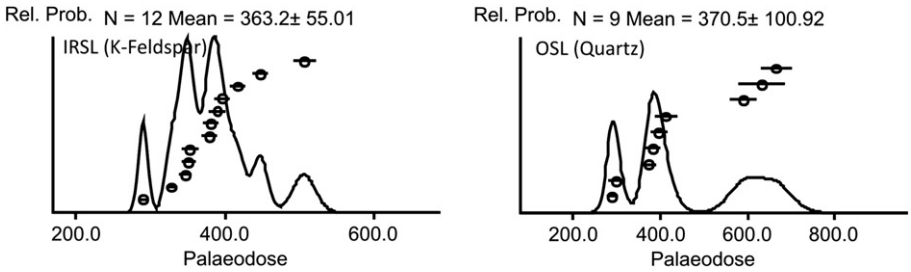

Fig. 9. Equivalent dose distribution diagrams for IRSL measurements of K-feldspar and OSL measurements of quartz. The x-axis represents the dose (expressed in seconds of exposure to a source providing ~5 Gy/s) required to reproduce the natural luminescence measured in the aliquot. The equivalent dose (De) for each aliquot is displayed in rank order and spread out along an arbitrary y-axis.

Table 2
Values used to calculate annual dose (for feldspar an internal dose was included in age estimation).

Sample	Grain size (μm)	Depth (m)	Water (%)	α-dose rate (Gy ka^{-1})	β-dose rate (Gy ka^{-1})	γ dose rate (Gy ka^{-1})	Cosmic dose rate (Gy ka^{-1})	K (%)	U (ppm)	Th (ppm)	Total dose rate (Gy/ka)
OSL	90–250	6.0 ± 0.05	2 ± 2	0.017 ± 0.008	0.438 ± 0.017	0.372 ± 0.011	0.226 ± 0.100	.324 ± 0.01	0.9 ± 0.01	4.2 ± 0.01	1.05 ± 0.10
KF	90–250	6.0 ± 0.05	2 ± 2	0.017 ± 0.008	0.875 ± 0.018	0.76 ± 0.03	0.226 ± 0.100	.324 ± 0.01	0.9 ± 0.01	4.2 ± 0.01	1.49 ± 0.14

The CRE data do not provide an independent constraint on the age of Sardar alluvial fan. However these data, when combined with the luminescence results indicate that the erosion rate on the sampled surface is high (>340 mm/ka; see Table 5) and at least three times higher than the mean erosion rate in the source area of Sardar alluvial deposits (~110 mm/ka; see previous paragraph).

7.2. Slip-rate estimate for the Tabas thrust fault

In the previous section, we have shown that anticlinal folding above a blind thrust fault has deformed the surface of an alluvial fan, the surface of which was likely abandoned at 12.5 ± 1.3 ka by the Sardar River. Constraints from the exposed geology, from the source parameters of earthquakes, and the shape of the deformation of the fan surface itself all provide a broadly consistent picture of slip on a gently (~20°) eastward-dipping thrust. From the exposed geology, this thrust is likely to shallow into a horizontal detachment at depths of only ~2 km. However, body-waveform models of earthquakes in 1978, 1979 and 1980 all show centroid depths of ~10 km (Walker et al., 2003), indicating that the rupture must have propagated to depths of considerably greater than 10 km. Presumably, the thrust faults that underlie the Tabas folds steepen beneath the Shotori Mountains into deeper structures, which also failed in the earthquakes, but which do not reach the surface.

The inferred age estimates of 12.5 ± 1.3 ka for the Sardar fan surface enable us to suggest a rate of <1 mm/yr of peak surface uplift above the Sardar anticline. Obtaining estimates of the slip-rate on the underlying thrust fault, and of the rate of horizontal shortening, are, however, made difficult because the main seismogenic fault does not reach the surface. If we assume that lateral transport of material on the horizontal decollement at depth is balanced by extrusion of material at the surface, we can produce approximate measurements of slip-rate and shortening by using area balancing (Fig. 11). The cross-sectional area of the fold in the F1 fan surface is ~32,500 m^2. With a decollement depth of 2 km, this yields a horizontal shortening of ~16 m. As the F1 surface is likely to be 12.5 ± 1.3 ka in age, the rate of horizontal shortening is hence ~1.2–1.4 mm/yr. If the surface abandonment postdates our minimum De OSL age, the rate of shortening will be slightly higher.

Table 3
Optical (OSL) and Infra-red stimulated luminescence (IRSL) age calculations from the abandoned alluvial fan (F1) of the Sardar River. Results are shown for weighted-mean, central, and minimum De age models. All experiments are from 90 to 250 μm-diameter grains collected at a depth of 0.6 ± 0.05 m from a sample pit at 33°39′12.9″N 57°05′54.4″E. Dose rates were calculated using the parameters shown in Table 2. Equivalent doses were calculated from the experimental procedures as described in the text.

Dating method	Age model	Dose rate (Gy/ka)	De (Gy)	Age (ka)
OSL (quartz)	Weighted mean	1.1 ± 0.1	28.8 ± 7.9	27.3 ± 8.0
IRSL (K-feldspar)	Weighted mean	1.5 ± 0.1	28.3 ± 4.3	19.0 ± 3.4
OSL (quartz)	Minimum De	1.1 ± 0.1	13.2 ± 0.4	12.5 ± 1.3
IRSL (K-feldspar)	Minimum De	1.5 ± 0.1	22.6 ± 0.5	15.2 ± 1.2
OSL (quartz)	Central age	1.1 ± 0.1	29.7 ± 2.3	28.2 ± 3.6
IRSL (K-feldspar)	Central age	1.5 ± 0.1	28.7 ± 1.0	19.3 ± 1.6

7.3. Right-lateral slip-rate on the Nayband Fault

The Tabas Fault system is situated near the northern end of the N–S right-lateral Nayband Fault (Fig. 1). The Nayband Fault is one of the longest active faults in Iran. It has no record of earthquakes but given its length, and its lack of segmentation, it has the potential to rupture in large magnitude earthquakes (Berberian and Yeats, 1999). As the Tabas and Nayband faults are closely associated spatially, information about the tectonics of the Tabas region is also helpful towards understanding the tectonics of the Nayband Fault, and hence of eastern Iran in general. A slip-rate of 1.5 ± 0.4 mm/yr is estimated for the central Nayband Fault from the displacement of 2.2-Ma-old basalts by Walker et al. (2009).

Fig. 12 shows the Nayband strike–slip fault close to where it enters the southern Shotori Mountains. The fault cuts across, and displaces, the surfaces of a series of alluvial fans originating from westward-flowing rivers (Fig. 12B). Restoration of 22 m of right-lateral slip realigns small distributary channels in the fan surfaces to linear, and presumably original, courses (Fig. 12C). Right-lateral strike–slip faulting continues farther north along the range-front of the Shotori Mountains, and there are a number of locations where cumulative right-lateral displacement of alluvial fan surfaces is observed (Figs. 2 and 13). What is noticeable about these sites is that the magnitude of the displacement in the fan surfaces appears to decrease northwards. At latitude 33°N a restoration of 11 m is required to restore drainage channels on a fan surface (Figs. 2 and 13A), and near latitude 33°10′N, close to the epicentre of the 1978 earthquake, only 6 m restoration is required (Figs. 2 and 13B).

Kilometre-scale right-lateral displacement of river courses is observed north of latitude 33°10′N (e.g. Fig. 10 of Walker et al., 2003), showing that significant amounts of strike–slip displacement have occurred along the Shotori range-front fault. However, displacements

Please cite this article as: Walker, R.T., et al., Co-seismic, geomorphic, and geologic fold growth associated with the 1978 Tabas-e-Golshan earthquake fault in eastern Iran, Geomorphology (2013), http://dx.doi.org/10.1016/j.geomorph.2013.02.016

Table 4
Composition of near-surface depth-profile Tabas samples obtained from prompt gamma activation analysis (PGAA), sodium peroxide fusion mass spectrometry (FUS-MS-Na_2O_2), isotope dilution and accelerator mass spectrometry (AMS–ID) and accelerator mass spectrometry (AMS). Sample numbers indicate depth in cm. Chemical species are arranged and scaled as required by Schimmelpfennig et al. (2009) spreadsheet.

Analyte symbol	Unit symbol	Detection limit	Analysis method	Samples										
				TABAS-0	TABAS-20	TABAS-40	TABAS-60	TABAS-80	TABAS-100	TABAS-120	TABAS-140	TABAS-160	TABAS-180	Mean and scatter
CaO	wt.%	−0.01	PGAA	25.80 ± 0.57	41.50 ± 0.79	37.90 ± 0.87	40.20 ± 0.84	43.93	45.75	44.91	42.40	45.60 ± 0.82	41.14	43 ± 2
			FUS-Na_2O_2											
K_2O	wt.%	−0.12	PGAA	0.234 ± 0.007	0.152 ± 0.005	0.230 ± 0.008	0.259 ± 0.007	0.24	<0.12	<0.12	0.12	0.159 ± 0.005	0.24	0.19 ± 0.04
			FUS-Na_2O_2											
TiO_2	wt.%	−0.02	PGAA	0.099 ± 0.003	0.058 ± 0.002	0.078 ± 0.003	0.119 ± 0.003	0.07	0.03	0.05	0.08	0.046 ± 0.001	0.08	0.07 ± 0.02
			FUS-Na_2O_2											
Fe_2O_3 (T)	wt.%	−0.07	PGAA	7.30 ± 0.17	0.62 ± 0.02	0.83 ± 0.03	1.11 ± 0.03	0.79	0.51	0.57	1.14	0.38 ± 0.01	2.75	1.2 ± 0.9
			FUS-Na_2O_2											
Cl	ppm	–	PGAA	145 ± 3	90 ± 2	86 ± 2	102 ± 2	95 ± 10	101 ± 10	100 ± 10	89 ± 9	68 ± 2	90 ± 9	96 ± 13
		–	AMS–ID	108 ± 11	89 ± 9	96 ± 10	120 ± 12					65 ± 7		
SiO_2	wt.%	−0.02	PGAA	38.60 ± 0.85	12.70 ± 0.27	23.40 ± 0.56	16.00 ± 0.37	9.01	5.78	7.60	10.65	9.60 ± 0.20	11.17	9 ± 2
			FUS-Na_2O_2											
Na_2O	wt.%	–	PGAA	0.22 ± 0.02	0.12 ± 0.01	0.23 ± 0.02	0.22 ± 0.01					0.12 ± 0.01		
MgO	wt.%	−0.02	PGAA	2.60 ± 0.13	4.10 ± 0.12	4.00 ± 0.15	4.80 ± 0.15	4.06	4.24	4.71	4.72	370 ± 0.14	4.49	4.4 ± 0.3
			FUS-Na_2O_2											
Al_2O_3	wt.%	−0.02	PGAA	1.58 ± 0.05	0.81 ± 0.03	1.24 ± 0.04	1.49 ± 0.04	1.15	0.66	0.74	1.23	0.73 ± 0.03	1.62	1.1 ± 0.3
			FUS-Na_2O_2											
MnO	wt.%	−0.0004	PGAA	700 ± 22	220 ± 9	280 ± 14	320 ± 13	0.02	0.01	0.01	0.03	200 ± 12	0.05	0.02 ± 0.02
			FUS-MS-Na_2O_2											
P_2O_5	wt.%	0.01	FUS-Na_2O_2					0.03	<0.01	<0.01	0.07		0.14	0.05 ± 0.05
CO_2	wt.%	–	PGAA	22 ± 2	39 ± 1	31 ± 2	35 ± 1					39 ± 1		33 ± 7
H_2O	wt.%	–	PGAA	1.482 ± 0.033	0.471 ± 0.009	0.614 ± 0.014	0.719 ± 0.015					0.443 ± 0.009		0.7 ± 4
Li	ppm	3	FUS-MS-Na_2O_2			6.99 ± 0.05		5	3	4	5		7	5 ± 1
B	ppm	−10	PGAA	15.17 ± 0.11	5.96 ± 0.04	0.83 ± 0.02	0.80 ± 0.06	20	30	20	30	4.67 ± 0.03	30	15 ± 3
			FUS-MS-Na_2O_2											
Sm	ppm	−0.1	PGAA	1.27 ± 0.03	0.52 ± 0.01	1.13 ± 0.03	0.82 ± 0.01	0.8	0.6	0.6	1.0	0.58 ± 0.02	1.3	0.8 ± 0.2
			FUS-MS-Na_2O_2											
Gd	ppm	−0.1	PGAA	1.69 ± 0.04	0.68 ± 0.02		1.00 ± 0.03	1.0	0.8	0.9	0.8	0.82 ± 0.02	1.5	1.0 ± 0.2
			FUS-MS-Na_2O_2											
Th	ppm	0.1	FUS-MS-Na_2O_2					1.0	0.8	0.9	4.1		2.4	2 ± 1
U	ppm	0.1	FUS-MS-Na_2O_2					<0.1	<0.1	<0.1	3.8		1.7	1 ± 1
Cr	ppm	30	FUS-MS-Na_2O_2					<30	<30	<30	<30		<30	15 ± 15
Be	ppm	3	FUS-MS-Na_2O_2					<3	<3	<3	<3		<3	1.5 ± 1.5
N								No data						
F								No data						
S	ppm	−10	PGAA	58 ± 4	250 ± 25	270 ± 32	330 ± 30	440	420	460	380	340 ± 44	380	442 ± 35
	ppm		FUS-MS-Na_2O_2											
Sc						29 ± 3		No data						
Co	ppm	−0.02	PGAA					0.70	<0.2	<0.2	1.00		2.60	5 ± 5
			FUS-MS-Na_2O_2											
Nl	ppm	10	FUS-MS-Na_2O_2					<10	<10	<10	<10		<10	5 ± 5
Se	ppm	0.8	FUS-MS-Na_2O_2					<0.8	<0.8	2.10	1.00	<0.8		0.9 ± 0.7
Br								No data						
Rb	ppm	0.4	FUS-MS-Na_2O_2					6.6	3.7	3.6	6.8		8.6	6 ± 2
Sr	ppm	3	FUS-MS-Na_2O_2					212	167	185	170		200	187 ± 19
Zr								No data						
Mo	ppm	1	FUS-MS-Na_2O_2					<1	19	<1	<1		<1	4 ± 4
Ru								No data						
Te	ppm	6	FUS-MS-Na_2O_2					<6	<6	<6	<6		<6	3 ± 3
I								No data						
Cs	ppm	0.1	FUS-MS-Na_2O_2					0.6	0.4	0.3	0.5		0.6	0.5 ± 0.1
Ba	ppm	3	FUS-MS-Na_2O_2					234	38	73	119		137	120 ± 75
^{36}Cl	10^3 at. g^{-1}	–	AMS[a]	1141 ± 62	1153 ± 62	1333 ± 79	1133 ± 93	1462 ± 75	1135 ± 71	1333 ± 66	1036 ± 66	1151 ± 69	1128 ± 70	1221 ± 134

[a] Analytical uncertainties (reported as 1σ) include uncertainties associated with accelerator mass spectrometry (AMS) counting statistics, AMS external error, and blank measurement errors.

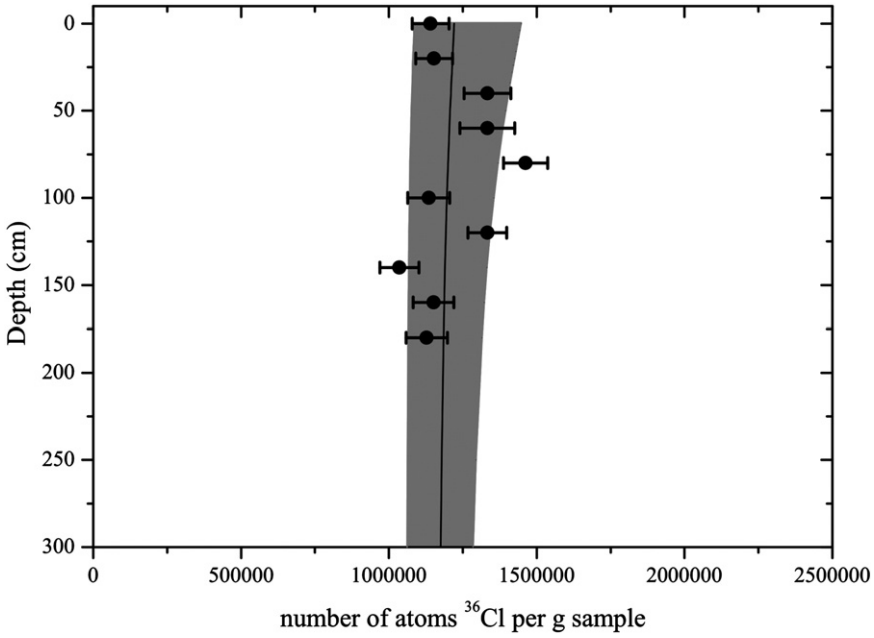

Fig. 10. Depth profile of ^{36}Cl concentrations at 20 cm intervals from the surface to a depth of 180 cm. Best fit model is indicated by a black line. Model results that fit the measured ^{36}Cl dataset within one sigma confidence level are depicted by the grey area. Model results indicate an inherited concentration of 1.1 ± 0.1 million ^{36}Cl atoms per gramme of sample.

Table 5
Monte Carlo simulations inputs and outputs. Results not constraining the parameters more than input limits are shown in italics. Two sets of simulations were made, the first one allows the parameters to vary in a wide window, and the second one constrains the age between 8 and 14 ka, according to independent IRSL and OSL measurements.

Model limits				Monte Carlo simulations		Model results				
$N_{inher.}$ (current) (10^3 at. g^{-1})	t (ka)	ε (mm ka^{-1})	ρ (g cm^{-3})	Total	Fitting 1σ	χ^2 Total (6 DOF)	$N_{inher.}$ (current) (10^3 at. g^{-1})	t (ka)	ε (mm ka^{-1})	ρ (g cm^{-3})
0–1500	0–2000	0–3000	1.5–2.7	10,000	243	30.3–32.9	1050–1219	*0–2000*	*0–3000*	*1.5–2.7*
0–1500	8–14	0–3000	1.5–2.7	12,000	370	30.9–33.5	1067–1216	*8–14*	340–*3000*	*1.5–2.7*

in late Quaternary alluvial fans do not show significant amounts of lateral displacement. For example, by latitude 33°30′N, no lateral displacement is visible at a range-front scarp in alluvial fans (Fig. 13C). The recent movement on the fault at this location appears instead to be reverse faulting and the curved trace of the fault suggests a significant dip to the east.

We have no direct constraints on the ages of the fans described above, and whether they are all of similar age, and so we cannot produce a firm estimate either of the magnitude of slip-rate at any one location, or of variations in the slip-rate between the sites. The observations that we have described do, however, suggest that the strike–slip component of slip becomes smaller to the north. Finally, we note that

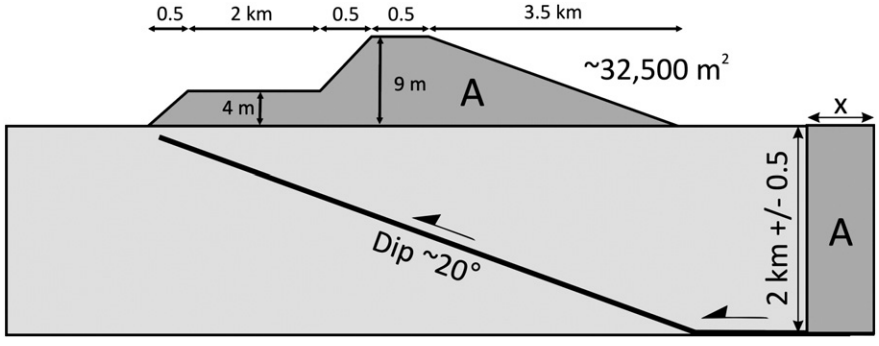

Fig. 11. Simplified cross-section showing the main features of the area-balancing slip-rate estimation. For the purpose of this calculation we have assumed that the Sardar Fault segment consists of a planar surface dipping 20° to the east and flattening into a horizontal detachment at a depth of 2 km. We have also assumed that there is no loss of cross-sectional area during the transport of material in the hanging-wall of the fault. The amount of horizontal shortening since the abandonment of the F1 fan surface (x) multiplied by the depth of the detachment (2 km) is equal to the region between the present-day deformed F1 fan surface and the original undeformed surface (area A). We approximate area A at ~32,500 m^2.

Please cite this article as: Walker, R.T., et al., Co-seismic, geomorphic, and geologic fold growth associated with the 1978 Tabas-e-Golshan earthquake fault in eastern Iran, Geomorphology (2013), http://dx.doi.org/10.1016/j.geomorph.2013.02.016

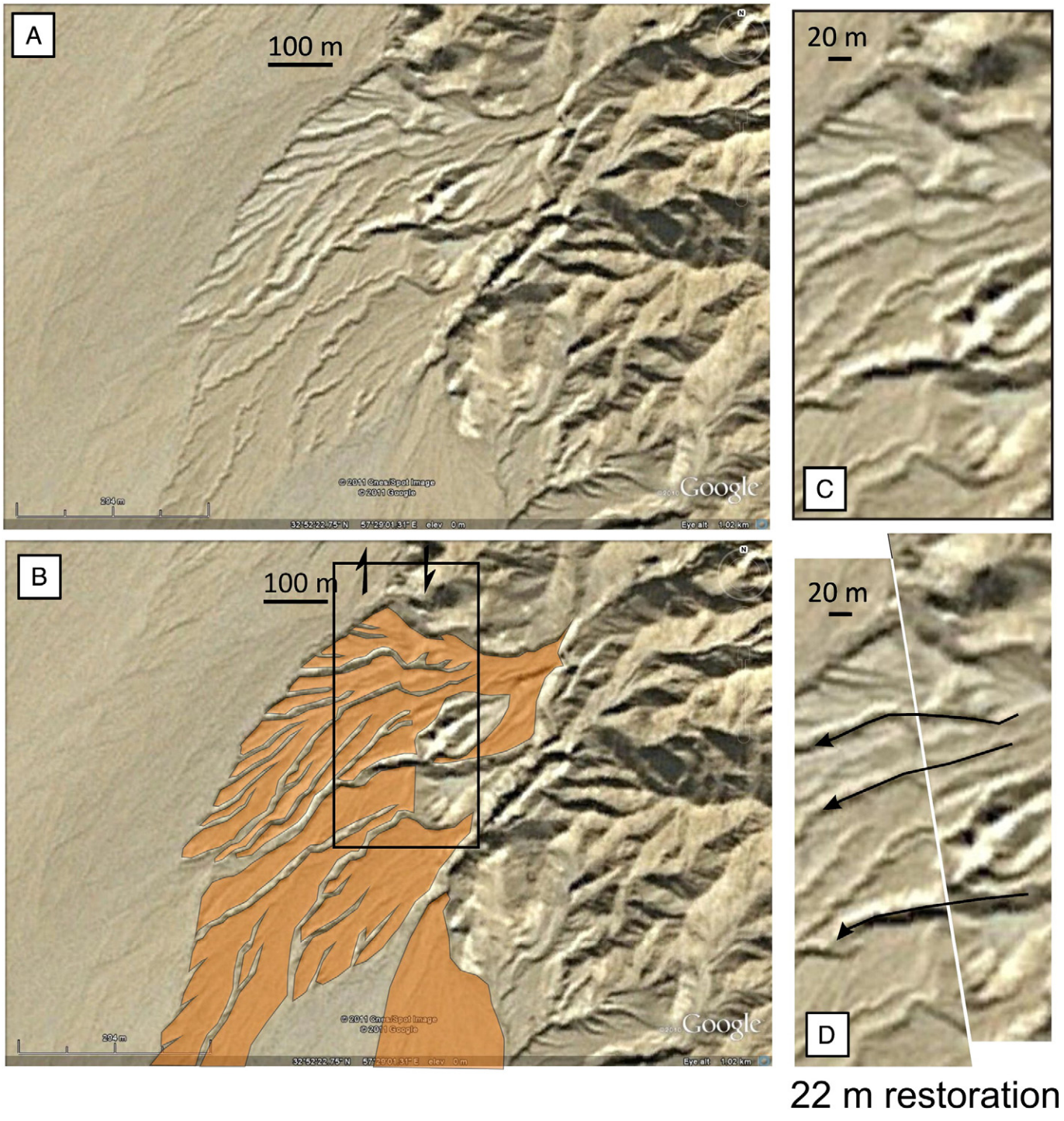

Fig. 12. (A) SPOT5 satellite image, from Google Earth, showing the Nayband Fault as it enters the southernmost Shotori Mountains (approximate centre location — 32°52′25″N 57°29′03″E; see Fig. 2 for location). The fault displaces the abandoned surface of an alluvial fan deposited from a westward-flowing river. (B) Interpretation of 'A'. The alluvial fan surface is highlighted in grey (orange in online version), the Nayband Fault location is marked by half-arrows. The box marks the region represented in 'C'. (C) Close-up of the fan surface where it is cut by the Nayband Fault. A series of small incised streams on the fan surface are displaced right-laterally across the fault. (D) The displaced streams are restored to their initial linear courses with 22 m of right-lateral slip removed.

the 22 m right-lateral displacement at the southernmost of our sites (Fig. 12) would accumulate in 11–20 ka at the rate of 1.1–1.9 mm/yr estimated for the Nayband Fault by Walker et al. (2009). It is possible, therefore, that the abandoned alluvial fans shown in Figs. 12 and 13 are similar in age to the 12.5 ± 1.3 ka Sardar fan, and represent a regionally extensive period of fan aggradation (e.g. Walker and Fattahi, 2011).

8. Discussion

The active faulting at Tabas is important for a number of reasons. It was the site of a devastating earthquake in 1978 and is potentially an important feature in the active tectonics of Iran. It is also an important region for understanding the tectonic and environmental controls on landscape development. Our study, which has combined seismological,

Please cite this article as: Walker, R.T., et al., Co-seismic, geomorphic, and geologic fold growth associated with the 1978 Tabas-e-Golshan earthquake fault in eastern Iran, Geomorphology (2013), http://dx.doi.org/10.1016/j.geomorph.2013.02.016

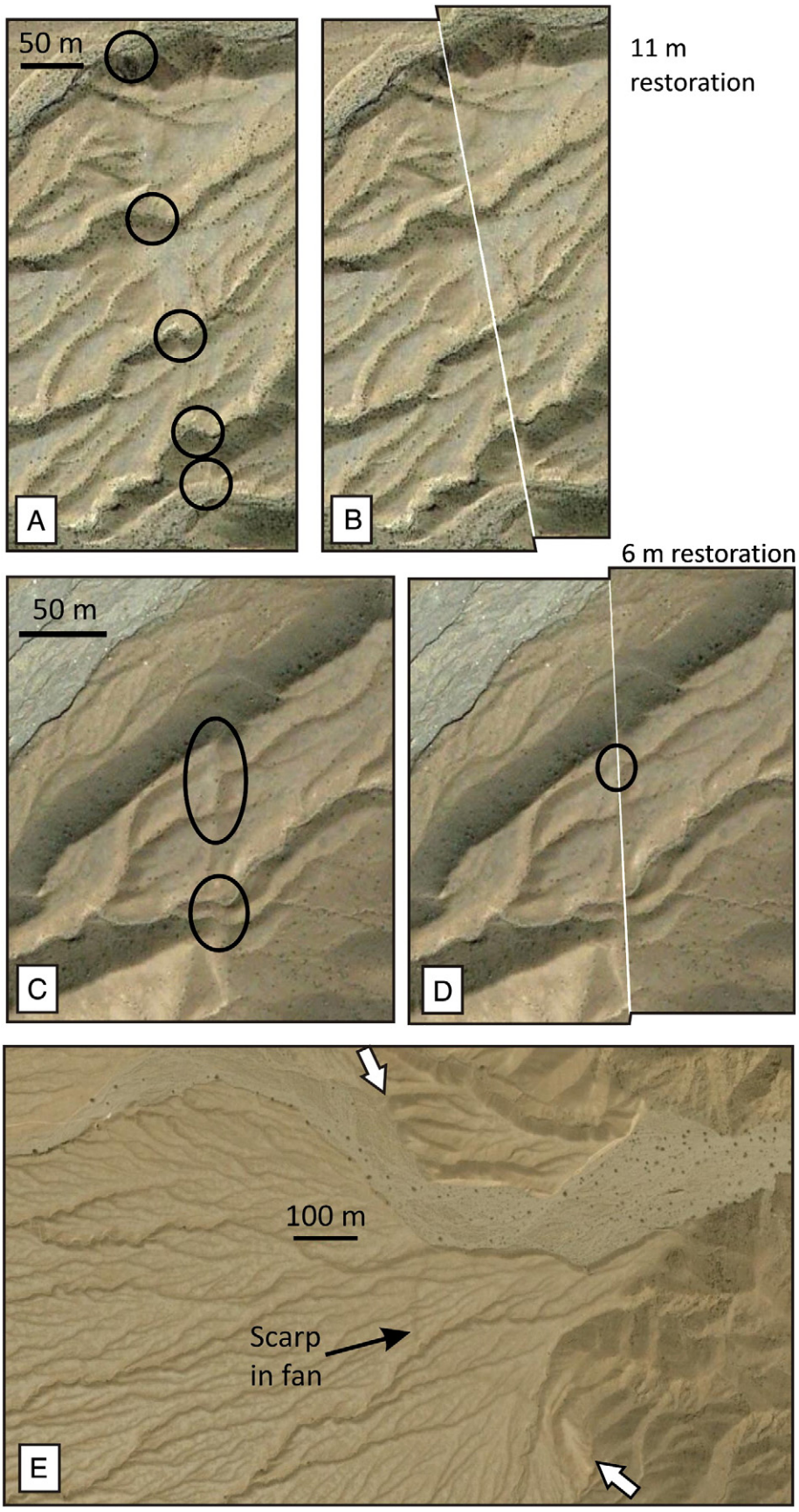

Fig. 13. SPOT5 imagery (from Google Earth) showing diminishing amounts of right-lateral displacement in young fan surfaces arranged from south to north. See Fig. 2 for locations. (A) A series of five incised streams and terrace risers (circled) all right-laterally displaced by 11 m (approximate centre location — 33°00′19″N 57°27′30″E). The restored drainage is shown in (B). (C) The courses of two incised streams (southern ellipse) and of a terrace riser (northern ellipse) are displaced right-laterally by 6 m (at 33°08′15″N 57°24′09″E). (D) Note that one stream (circled) still shows an apparent right-lateral displacement with the 6 m of slip restored. (E) Scarp in fan showing no discernible lateral displacement at 33°31′51″N 57°10′05″E. The scarp is convex to the west as it crosses the fan apex, indicating an eastward dip.

Please cite this article as: Walker, R.T., et al., Co-seismic, geomorphic, and geologic fold growth associated with the 1978 Tabas-e-Golshan earthquake fault in eastern Iran, Geomorphology (2013), http://dx.doi.org/10.1016/j.geomorph.2013.02.016

geological and geomorphological investigations, yields results relevant both to tectonics and to landscape evolution, and we deal with these two separately below.

8.1. Insights into the 1978 Tabas earthquake and the active tectonics of the Tabas region

We show that the Sardar anticline is consistent with the oblique right-lateral and reverse slip suggested by the focal mechanism of the 1978 earthquake. The right-lateral strike–slip component is accommodated by distributed deformation within the forelimb of the fold, either as oblique slip on bedding-plane faults or as steep strike–slip faults that cut through the fold limb. Distributed oblique slip in the hanging-wall of blind, or partially-blind, thrust faults was also seen following the 1957 Gobi–Altay earthquake in Mongolia (e.g. Bayasgalan et al., 1999), the 1980 El-Asnam earthquake in Algeria (e.g. Philip and Meghraoui, 1983), and the 1988 Spitak earthquake in Armenia (e.g. Philip et al., 1992). Changes in thickness of the F1 fan deposits across bedding-slip surfaces (e.g. Fig. 6B) show that although the bedding-plane faults slipped by only a few centimetres in the 1978 earthquake, they have accommodated considerable amounts of cumulative displacement.

The width of the Sardar anticline reveals that the underlying thrust fault is likely to flatten into a decollement at only ~2 km depth. As the centroid depth of the 1978 earthquake is nine kilometres, it is probable that it also involved rupture on deeper structures that remain hidden. Apart from in the southernmost part of the Shotori Mountains the faults at the range-front fault appear to be either inactive in the Holocene or to be predominantly dip–slip (e.g. Figs. 2 and 13). Kilometre-scale right-lateral river displacements are, however, visible near the range-front (e.g. Walker et al., 2003). This suggests that the faulting has evolved through time, with an initial period of oblique slip at the Shotori range-front, followed by a westwards migration of activity, at least in the upper two kilometres of the earth, towards the basin interior. The westward migration of activity is likely to have been aided by the presence of thick marl deposits that provide suitable detachment horizons. It is important to note that if the blind faults that underlie the Tabas folds link with a more steeply-dipping structure beneath the Tabas range-front it will introduce extension above the fault bend. The presence of seismicity within the Tabas playa might indicate that some shortening is accommodated on structures west of those visible in the geomorphology (Fig. 2).

Our detailed measurements are restricted to only one of the fold segments of the Tabas system and it is unclear to what extent our interpretations of detachment depth and accommodation of oblique slip in the fold forelimb are applicable to other parts of the system. The topographic expression of each of the other fold segments is either similar to, or narrower than, that of the Sardar segment (e.g. Fig. 2) suggesting that detachment depth might be similar. However, the segments north and south of Espahk village (Fig. 2) expose Mesozoic bedrock in their cores, suggesting either that the Cenozoic basin fill is extremely thin around Espahk, or that the thrust faults penetrate deeper.

In Fig. 14, we have drawn a sketch of the Tabas Fault system. The average strike of the Tabas folds, and of the range-front fault of the Shotori Mountains, is ~25° from the N–S trending Nayband Fault. If right-lateral strike–slip on the Nayband Fault is transferred northwards onto the Tabas and Shotori faults, the 1.1–1.9 mm/yr of right-lateral slip estimated for the Nayband Fault (Walker et al., 2009; Section 7.3), will be split into 1.0–1.7 mm/yr of right-lateral strike–slip parallel to the Shotori range, and 0.5–0.8 mm/yr of shortening orthogonal to the range.

From area balancing we estimated 1.2–1.4 mm/yr of shortening across the Sardar fold (Section 7.2). Although this independent estimate is slightly larger than the 0.5–0.8 mm/yr derived above, it is dependent on the depth at which the Sardar Fault flattens into a horizontal decollement; how well we have approximated the area 'A' in Fig. 11; and also in whether the assumption that the area 'A' in Fig. 11 is equal to the sum of decollement depth and horizontal shortening. Also, the 'slip-partitioning' method of estimating the rate of shortening is heavily dependent on the assumption that the 0.9–1.9 mm/yr estimate of slip-rate for the Nayband Fault, which is averaged over 2.2 Ma, is representative of the late Pleistocene slip-rate at the northern end of the Nayband Fault (Walker et al., 2009; Section 7.3).

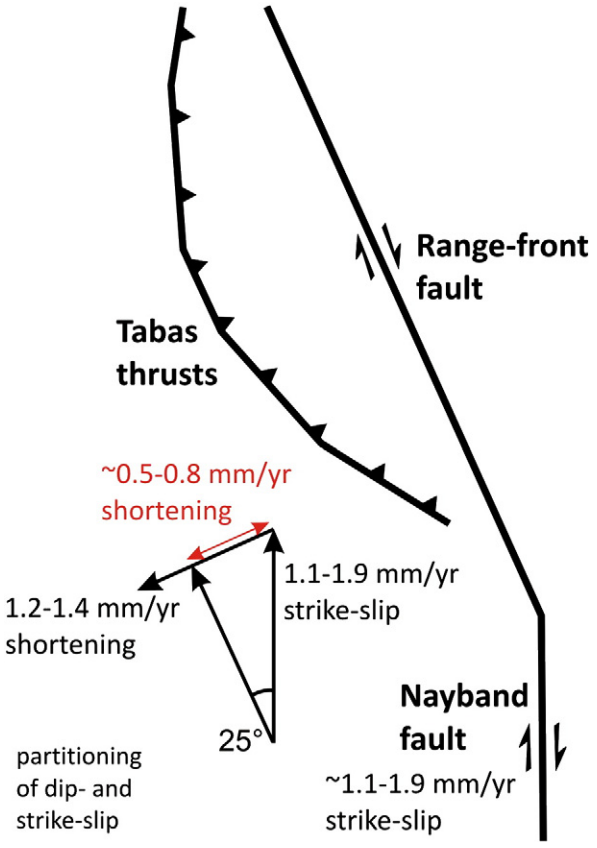

Fig. 14. If shortening across the Tabas thrusts is caused by transpressional bending along the northern Nayband Fault, right-lateral slip on the N–S Nayband Fault will be split into orthogonal components of right-lateral strike–slip (accommodated on faults in the Shotori Mountains and within the Tabas folds themselves), and shortening. The estimated right-lateral slip rate on the N–S Nayband Fault is 1.1–1.9 mm/yr (Walker et al., 2009; see Section 7.3) such that the shortening across the Tabas Faults should be 0.5–0.8 mm/yr. The rate of shortening estimated from deformation of the F1 fan is 1.2–1.4 mm/yr (Section 7.2).

Nonetheless, it appears as though 0.5–1.4 mm/yr of horizontal shortening is accommodated across the Shotori range-front and Tabas Faults. At the slowest end of this range, 0.5 mm/yr of shortening implies 1.0 mm/yr of right-lateral strike–slip, whilst at the fastest end, 1.4 mm/yr of shortening implies 3.0 mm/yr of strike–slip. A proportion of this strike–slip is likely to be accommodated across the Tabas Faults themselves, as indicated both by the focal mechanisms of the earthquakes (Walker et al., 2003), and by the distributed oblique slip observed within the hanging-wall of the Sardar Fault (Section 5). The Shotori range-front fault and, potentially, additional unknown faults within the interior of the Shotori Mountains might also contribute towards accommodation of the total slip across the zone.

8.2. Landscape evolution in the Tabas region

The Sardar River is one of the most striking elements of the landscape around Tabas (Figs. 3 and 15). This river, which occupies a

Please cite this article as: Walker, R.T., et al., Co-seismic, geomorphic, and geologic fold growth associated with the 1978 Tabas-e-Golshan earthquake fault in eastern Iran, Geomorphology (2013), http://dx.doi.org/10.1016/j.geomorph.2013.02.016

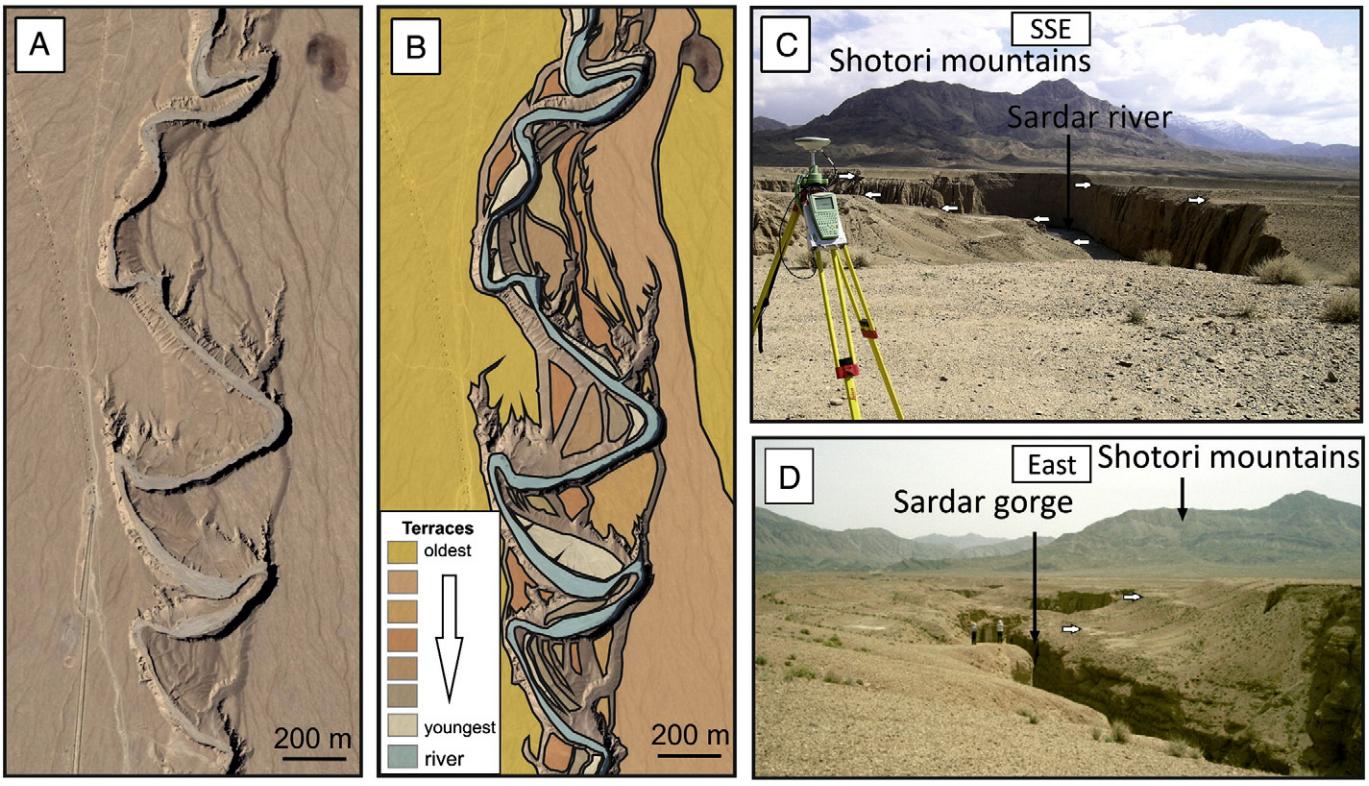

Fig. 15. (A) Quickbird satellite image (from Google Earth) showing terraces of the Sardar River set into the F1 fan surface (approximate centre location — 33°39′08″N 57°06′11″E; see Fig. 3 for location). (B) Interpretation of 'A'. (C) and (D) Field photographs showing views into the Sardar canyon (approximate locations 33°39′14″N 57°06′00″E and 33°38′30″N 57°05′05″E respectively). Several of the river terraces are visible (marked by white arrows).

canyon up to 100 m deep, has a large catchment within the Shotori Mountains. The incision of the Sardar River ends at the western flank of the Sardar anticline; a pattern of incision that was initially interpreted to result from cumulative hanging-wall uplift above the eastward-dipping thrust fault responsible for the 1978 earthquake (Walker et al., 2003).

Our measurements of deformation across the fan (F1) into which the Sardar River has incised show that uplift above the Sardar blind thrust fault is only responsible for ~10 m of the 100 m of incision of the Sardar River. The river incision is not, therefore, purely a result of deformation of the surface of the fan and the major part of the incision may instead be controlled by environmental factors. Walker and Fattahi (2011) propose a scenario of environmental change in the late Quaternary of eastern Iran that may account for the deep incision of the Sardar canyon. In their scenario, large alluvial fans were deposited in the latest Pleistocene and early Holocene during a time of abundant sediment supply. The rivers then incised into their fan deposits as sediment supply decreased.

The walls of the Sardar canyon are lined with excavations. Stöcklin et al. (1965) suggest that the cave dwellings were originally constructed at or near the level of the riverbed and have since achieved their precarious heights on the canyon walls due to lowering of the riverbed after their construction. We consider this scenario to be unlikely. Firstly, in order for the dwellings to be preserved it would require the canyon to have been cut without any lateral erosion of its walls. Furthermore, many of the excavations were constructed during the Arab invasion of 636–652 A.D. (M. Berberian, pers. comm., 2012; Fig. 16B), and were cut into the canyon walls at the tops of steep talus slopes, in locations that appear to have been chosen to be difficult, though not impossible, to access (Fig. 16C). Also, the excavations include narrow vertical shafts that lead to upper galleries opening onto higher levels of the canyon wall (M. Berberian, pers. comm., 2012).

We found one location where late Holocene lowering of the riverbed could be reliably inferred. At this site the Gholat fortress (an Assassin's castle of the 11th Century A.D.; M. Berberian, pers. comm., 2012) is sited on a promontory of the F1 fan surface between two tributaries of the Sardar River (Fig. 16A). A tunnel diverting water from the southern tributary to the northern one passes directly beneath the fortress, and a well shaft has been excavated in order to access the flowing water in the tunnel. Fig. 16D is a photograph of the northern entrance to the tunnel, which is ~7 m high. It is improbable that the tunnel was originally excavated at this height, and we speculate that instead the floor of the tunnel has been periodically lowered as a response to lowering of the natural riverbed.

9. Conclusions

The seismological, geomorphological and geological constraints on the structure of the Tabas blind thrusts help to constrain the subsurface structure of the faults and hence the source of the devastating 1978 earthquake. The Tabas Faults are likely to flatten into a decollement at a shallow depth and, in addition to faulting on the Tabas blind thrusts, the 1978 earthquake is likely to have involved rupture on deeper parts of the fault system beneath the Shotori Mountains. A component of strike–slip is accommodated by distributed deformation within the forelimb of the anticline. Folding of an alluvial fan surface across the Sardar anticline suggests that several blind thrust earthquakes have occurred in the Holocene. Faults at the Shotori range-front, which did not rupture at the surface in the 1978 earthquake, show evidence for activity in the Holocene and may constitute an additional hazard. Finally, we have shown that the active tectonics plays a secondary role to environment in shaping the Holocene landscape evolution at Tabas.

Please cite this article as: Walker, R.T., et al., Co-seismic, geomorphic, and geologic fold growth associated with the 1978 Tabas-e-Golshan earthquake fault in eastern Iran, Geomorphology (2013), http://dx.doi.org/10.1016/j.geomorph.2013.02.016

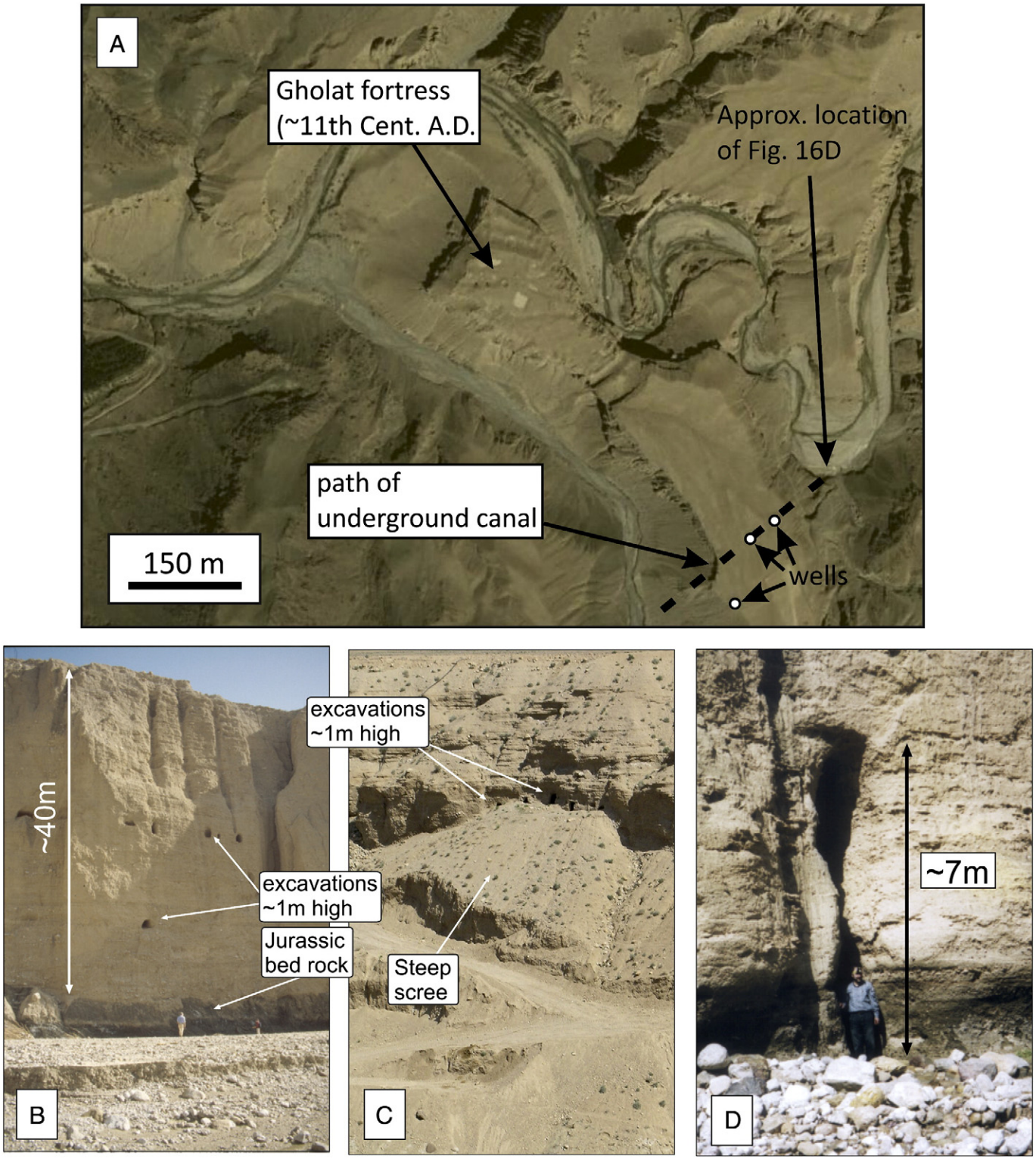

Fig. 16. (A) Quickbird satellite image (from Google Earth, approximate centre location — 33°39′17″N 57°09′06″E) of the Sardar River canyon close to the village of Kharv-e Bala in the Shotori Mountains. An 11th Century A.D. fortress (M. Berberian, pers. comm., 2012) is sited on the F1 terrace surface at the confluence of two tributaries of the Sardar River. A source of water is provided by an underground canal running between the two tributaries that is tapped by wells on the terrace. (B) View of the Canyon walls of the Sardar River near Kharv-e Bala (exact location unknown). Excavations are visible at various levels. (C) Excavations high on the Sardar canyon walls (close to the range-front of the Shotori Mountains, exact location unknown) accessed by a traverse along a steep scree cone. (D) Outlet of the underground canal shown in 'A'. The tunnel is ~7 m deep. It is probable that the base of the canal has been deepened in response to lowering of the river-bed (approximate location shown in part 'A').

Acknowledgements

We thank the University of Birjand, the Geological Survey of Iran, and the local government of Tabas for their support of this project. We are grateful to Mr. Arabi and Mr. Califi for their careful driving during the two field visits to Tabas. We also express our thanks to A. Dolati and R. Tajik for their help in making the GPS measurements. Accelerator Mass Spectrometer measurements were performed by

Please cite this article as: Walker, R.T., et al., Co-seismic, geomorphic, and geologic fold growth associated with the 1978 Tabas-e-Golshan earthquake fault in eastern Iran, Geomorphology (2013), http://dx.doi.org/10.1016/j.geomorph.2013.02.016

Colin Maden at SUERC, and the AMS data reduction by Stewart Freeman and Colin Maden. RTW is funded through a University Research Fellowship from the Royal Society of London though the fieldwork was undertaken whilst he was supported by a NERC Postdoctoral Fellowship. We thank Manuel Berberian and an anonymous reviewer for detailed and helpful comments.

References

Ambraseys, N.N., Melville, C.P., 1982. A History of Persian Earthquakes. Cambridge University Press, Cambridge, UK (219 pp.).

Bayasgalan, A., Jackson, J., Ritz, J.-F., Carretier, S., 1999. Forebergs, flower structures, and the development of large intracontinental strikeslip faults: the Gurvan Bogd Fault system in Mongolia. Journal of Structural Geology 21, 1285–1302.

Berberian, M., 1979. Earthquake faulting and bedding thrust associated with the Tabas-e-Golshan (Iran) earthquake of September 16, 1978. Bulletin of the Seismological Society of America 69, 1861–1887.

Berberian, M., 1982. Aftershock tectonics of the 1978 Tabas-e-Golshan (Iran) earthquake sequence: a documented active 'thin- and thick-skinned tectonic' case. Geophysical Journal of the Royal Astronomical Society 68, 499–530.

Berberian, M., Yeats, R.S., 1999. Patterns of historical earthquake rupture in the Iranian Plateau. Bulletin of the Seismological Society of America 89, 120–139.

Berberian, M., Asudeh, I., Bilham, R.G., Scholz, C.H., Soufleris, C., 1979. Mechanism of the main shock and the aftershock study of the Tabas-e-Golshan (Iran) earthquake of September 16, 1978: a preliminary report. Bulletin of the Seismological Society of America 69, 1851–1859.

Camp, V.E., Griffis, R.J., 1982. Character, genesis and tectonic setting of igneous rocks in the Sistan suture zone, eastern Iran. Lithos 3, 221–239.

Daeron, M., Avouac, J.P., Charreau, J., Dominguez, S., 2007. Modeling the shortening history of a fault-tip fold using structural and geomorphic records of deformation. Journal of Geophysical Research 112, B03S13. http://dx.doi.org/10.1029/1006JB004460.

Duller, G.A.T., 2008. Single-grain optical dating of Quaternary sediments: why aliquot size matters in luminescence dating. Boreas 37, 589–612. http://dx.doi.org/10.1111/j.1502-3885.2008.00051.x.

Engdahl, E.R., van der Hilst, R., Buland, R., 1998. Global teleseismic earthquake relocation with improved travel times and procedures for depth determination. Bulletin of the Seismological Society of America 88, 722–743.

Fattahi, M., Walker, R., Hollingsworth, J., Bahroudi, A., Nazari, H., Talebian, M., Armitage, S., Stokes, S., 2006. Holocene slip-rate on the Sabzevar thrust fault, NE Iran, determined using optically stimulated luminescence (OSL). Earth and Planetary Science Letters 245, 673–684.

Fattahi, M., Walker, R.T., Talebian, M., Sloan, R.A., Rasheedi, A., 2011. The structure and Late Quaternary slip-rate of the Rafsanjan strike–slip fault, SE Iran. Geosphere 7, 1159–1174.

Galbraith, R.F., Roberts, R.G., Laslett, G.M., Yoshida, H., Olley, J.M., 1999. Optical dating of single and multiple grains of quartz from Jinmium rock shelter, northern Australia: part I. Experimental design and statistical models. Archaeometry 41, 339–364. http://dx.doi.org/10.1111/j.1475-4754.1999.tb00987.x.

Ghods, A., Rezapour, M., Bergman, E., Mortezanejad, G., Talebian, M., 2012. Relocation of the 2006 Mw 6.1 Silakhour, Iran, earthquake sequence: details of fault segmentation on the main recent fault. Bulletin of the Seismological Society of America 102, 398–416.

Jackson, J., McKenzie, D., 1984. Active tectonics of the Alpine–Himalayan belt between Turkey and Pakistan. Geophysical Journal of the Royal Astronomical Society 77, 185–264.

Jordan, T.H., Sverdrup, K.A., 1981. Teleseismic location techniques and their application to earthquake clusters in the south-central Pacific. Bulletin of the Seismological Society of America 71, 1105–1130.

Le Dortz, K., Meyer, B., Sebrier, M., Nazari, H., Braucher, R., Fattahi, M., Benedetti, L., Foroutan, M., Siame, L., Bourles, D., Talebian, M., Bateman, M.D., Ghoraishi, M., 2009. Holocene right-slip rate determined by cosmogenic and OSL dating on the Anar Fault, Central Iran. Geophysical Journal International 179, 700–710.

Le Dortz, K., Meyer, B., Sébrier, M., Braucher, R., Nazari, H., Benedetti, L., Fattahi, M., Bourles, D., Foroutan, M., Siame, L., Rashidi, A., Bateman, M.D., 2011. Dating inset terraces and offset fans along the Dehshir Fault combining cosmogenic and OSL methods. Geophysical Journal International 185, 1147–1174. http://dx.doi.org/10.1111/j.1365-246X.2011.05010.

Maden, C., Anastasi, P.A.F., Dougans, D., Freeman, S.P.H.T., Kitchen, R., Klody, G., Schnabel, C., Sundquist, M., Vanner, K., Xu, S., 2007. SUERC AMS ion detection. Proceedings of the 10th Conference on Accelerator Mass Spectrometry: Nucl. Instr. and Meth. B, 259, pp. 131–139.

Meyer, B., LeDortz, K., 2007. Strike–slip kinematics in Central and Eastern Iran: estimating fault slip-rates averaged over the Holocene. Tectonics 26, TC5009. http://dx.doi.org/10.1029/2006TC002073.

Meyer, B., Mouthereau, F., Lacombe, O., Agard, P., 2006. Evidence of Quaternary activity along the Deshir Fault: implication for the Tertiary tectonics of Central Iran. Geophysical Journal International 164, 192–201.

Murray, A.S., Wintle, A.G., 2000. Luminescence dating of quartz using an improved single-aliquot regenerative-dose protocol. Radiation Measurements 32, 57–73.

Niazi, M., Kanamori, H., 1981. Source parameters of 1978 Tabas and 1979 Qainat, Iran, earthquakes from long-period surface waves. Bulletin of the Seismological Society of America 71, 1201–1213.

Parsons, B., Wright, T., Rowe, P., Andrews, J., Jackson, J., Walker, R., Khatib, M., Talebian, M., Bergman, E., Engdahl, E.R., 2006. The 1994 Sefidabeh (eastern Iran) earthquakes revisited: new evidence from satellite radar interferometry and carbonate dating about the growth of an active fold above a blind thrust fault. Geophysical Journal International 164, 202–217.

Philip, H., Meghraoui, M., 1983. Structural analysis and interpretation of the surface deformations of the El Asnam Earthquake of October 10, 1980. Tectonics 2, 17–49.

Philip, H., Rogozhin, E., Cisternas, A., Bousquet, J.C., Borisov, B., Karakhanian, A., 1992. The Armenian earthquake of 1988 December 7: faulting and folding, neotectonics and palaeoseismicity. Geophysical Journal International 110, 141–158.

Regard, V., Bellier, O., Braucher, R., Gasse, F., Bourles, D., Mercier, J., Thomas, J.-C., Abbassi, M.R., Shabanian, E., Soleymani, Sh., 2005. 10Be dating of alluvial deposits from Southeastern Iran (the Hormoz Strait area). Palaeogeography, Palaeoclimatology, Palaeoecology 242, 36–53.

Rodés, A., Pallàs, R., Braucher, R., Moreno, X., Masana, E., Bourles, D.L., 2011. Effect of density uncertainties in cosmogenic ^{10}Be depth-profiles: dating a cemented pleistocene alluvial fan (Carboneras Fault, SE iberia). Quaternary Geochronology 6, 186–194.

Sarkar, I., Sriram, V., Hamzehaloo, H., Khattri, K.N., 2004. Sub-event analysis for the Tabas earthquake of September 16, 1978 using near field SH data. Physics of the Earth and Planetary Interiors 151, 53–76.

Schimmelpfennig, I., Benedetti, L., Finkel, R., Pik, R., Blard, P.-H., Bourlès, D., Burnard, P., Williams, A., 2009. Sources of in-situ ^{36}Cl in basaltic rocks. Implications for calibration of production rates. Quaternary Geochronology 4, 441–461.

Shoja-Taheri, J., Anderson, J.G., 1988. The 1978 Tabas, Iran, earthquake: an interpretation of the strong motion records. Bulletin of the Seismological Society of America 78, 142–171.

Silver, P.G., Jordan, T.H., 1983. Total-moment spectra of fourteen large earthquakes. Journal of Geophysical Research 88, 3273–3293.

Stöcklin, J., Nabavi, M.H., 1969. Geological Quadrangle Map of Iran, 1:250,000 scale, Boshruyeh Sheet (No. J7), Geological Survey of Iran, Tehran, Iran.

Stöcklin, J., Eftekhar-Nezhad, J., Hushmand-Zadeh, A., 1965. Geology of the Shotori Range (Tabas area, East Iran), Geological Survey of Iran, Report No. 3 (133 pp.).

Stone, J.O., 2000. Air pressure and cosmogenic isotope production. Journal of Geophysical Research 105, 753–759.

Stone, J.O.H., Allan, G.L., Fifield, L.K., Cresswell, R.G., 1996. Cosmogenic chlorine-36 from calcite spallation. Geochimica et Cosmochimica Acta 60, 679–692.

Tatar, M., Jackson, J., Hatzfeld, D., Bergman, E., 2007. The 2004 May 28 Baladeh earthquake (Mw 6.2) in the Alborz, Iran: overthrusting the South Caspian Basin margin, partitioning of oblique convergence and the seismic hazard of Tehran. Geophysical Journal International 170, 249–261.

Vernant, Ph., Nilforoushan, F., Hatzfeld, D., Abbassi, M.R., Vigny, C., Masson, F., Nankali, H., Martinod, J., Ashtiani, A., Bayer, R., Tavakoli, F., Chery, J., 2004. Present-day crustal deformation and plate kinematics in the Middle East constrained by GPS measurements in Iran and northern Oman. Geophysical Journal International 157, 381–398.

Vincent, P.J., Wilson, P., Lord, T.C., Schnabel, C., Wilcken, K.M., 2010. Cosmogenic isotope (^{36}Cl) surface exposure dating of the Norber erratics, Yorkshire Dales: further constraints on the timing of the LGM deglaciation in Britain. Proceedings of the Geologists' Association 121, 24–31. http://dx.doi.org/10.1016/j.pgeola.2009.12.009.

Walker, R.T., Fattahi, M., 2011. A framework of Holocene and Late Pleistocene environmental change in eastern Iran inferred from the dating of periods of alluvial fan abandonment, river terracing, and lake deposition. Quaternary Science Reviews 30, 1256–1271.

Walker, R., Jackson, J., 2002. Offset and evolution of the Gowk Fault, S.E. Iran: a major intra-continental strike–slip system. Journal of Structural Geology 24, 1677–1698.

Walker, R., Jackson, J., 2004. Active tectonics and late Cenozoic strain distribution in central and eastern Iran. Tectonics 23, TC5010. http://dx.doi.org/10.1029/2003TC001529.

Walker, R., Jackson, J., Baker, C., 2003. Surface expression of thrust faulting in eastern Iran: source parameters and surface deformation of the 1978 Tabas and 1968 Ferdows earthquake sequences. Geophysical Journal International 152, 749–765.

Walker, R.T., Bergman, E., Jackson, J., Ghorashi, M., Talebian, M., 2005. The 22 June 2002 Changureh (Avaj) earthquake in Qazvin province, NW Iran: epicentral re-location, source parameters, surface deformation and geomorphology. Geophysical Journal International 160, 707–720.

Walker, R.T., Gans, P., Allen, M.B., Jackson, J., Khatib, M., Marsh, N., Zarrinkoub, M., 2009. Late Cenozoic volcanism and rates of active faulting in eastern Iran. Geophysical Journal International 177, 783–805.

Walker, R.T., Talebian, M., Sloan, R.A., Rasheedi, A., Fattahi, M., Bryant, C., 2010. Holocene slip-rate on the Gowk strike–slip fault and implications for the distribution of tectonic strain in eastern Iran. Geophysical Journal International 181, 221–228. http://dx.doi.org/10.1111/j.1365-246X.2010.04538.x.

Walker, R.T., Bergman, E.A., Szeliga, W., Fielding, E.J., 2011. Insights into the 1968–1997 Dasht-e-Bayaz and Zirkuh earthquake sequences, eastern Iran, from calibrated relocations, InSAR and high-resolution satellite imagery. Geophysical Journal International 187, 1577–1603. http://dx.doi.org/10.1111/j.1365-246X.2011.05213.x.

Please cite this article as: Walker, R.T., et al., Co-seismic, geomorphic, and geologic fold growth associated with the 1978 Tabas-e-Golshan earthquake fault in eastern Iran, Geomorphology (2013), http://dx.doi.org/10.1016/j.geomorph.2013.02.016